Journal of Nanobiotechnology

RESEARCH Open Access

An injectable multifunctional nanocomposite hydrogel promotes vascularized bone regeneration by regulating macrophages

Huaiyuan Zhang[1†], Yu Wang[1†], Wenyu Qiao[2†], Xueneng Hu[1†], Huifen Qiang[3], Kuo Xia[1], Longhai Du[1], Luling Yang[4], Yi Bao[5], Jie Gao[3,6*], Tinglin Zhang[3,6*] and Zuochong Yu[1*]

Abstract

The local inflammatory microenvironment, insufficient vascularization, and inadequate bone repair materials are the three key factors that constrain the repair of bone defects. Here, we synthesized a composite nanoparticle, TPQ (TCP-PDA-QK), with a core–shell structure. The core consists of nanotricalcium phosphate (TCP), and the shell is derived from polydopamine (PDA). The surface of the shell is modified with a vascular endothelial growth factor (VEGF) mimic peptide (QK peptide). TPQ was then embedded in porous methacrylate gelatin (GelMA) to form a TPQGel hydrogel. In the inflammatory environment, the TPQGel hydrogel can gradually release drugs through pH responsiveness, promoting M2 macrophage polarization, vascularization and bone regeneration in turn. In addition, reprogrammed M2 macrophages stimulate the generation of anti-inflammatory and pro-healing growth factors, which provide additional support for angiogenesis and bone regeneration. The TPQGel hydrogel can not only accurately fill irregular bone defects but also has excellent biocompatibility, making it highly suitable for the minimally invasive treatment of bone defects. Transcriptomic tests revealed that the TPQGel hydrogel achieved macrophage reprogramming by regulating the PI3K-AKT signalling pathway. Overall, the TPQGel hydrogel can be harnessed for safe and efficient therapeutics that accelerate the repair of bone defects.

Keywords Inflammatory microenvironment, Bone defects, Core–shell structure, M2 macrophage polarization, Vascularization, Bone regeneration

Introduction

Bone defect reconstruction remains a significant clinical challenge in orthopedics, particularly following traumatic injury, tumor resection, or osteomyelitis debridement. While conventional approaches, including autografts, allografts, and synthetic bone substitutes, provide partial solutions, these strategies face persistent limitations, such as donor site morbidity, immunogenic responses, and inadequate vascular integration [1]. Current research indicates that macrophage polarization plays a pivotal role in the process of bone healing. In the early stages of bone healing, promoting the timely switch of macrophages to the M2 phenotype can create a favourable

†Huaiyuan Zhang, Yu Wang, Wenyu Qiao and Xueneng Hu contributed equally to this work.

*Correspondence:
Jie Gao
gaojiehighclea@smmu.edu.cn
Tinglin Zhang
ztl2107@smmu.edu.cn
Zuochong Yu
tjyd327@163.com

Full list of author information is available at the end of the article

Graphical Abstract

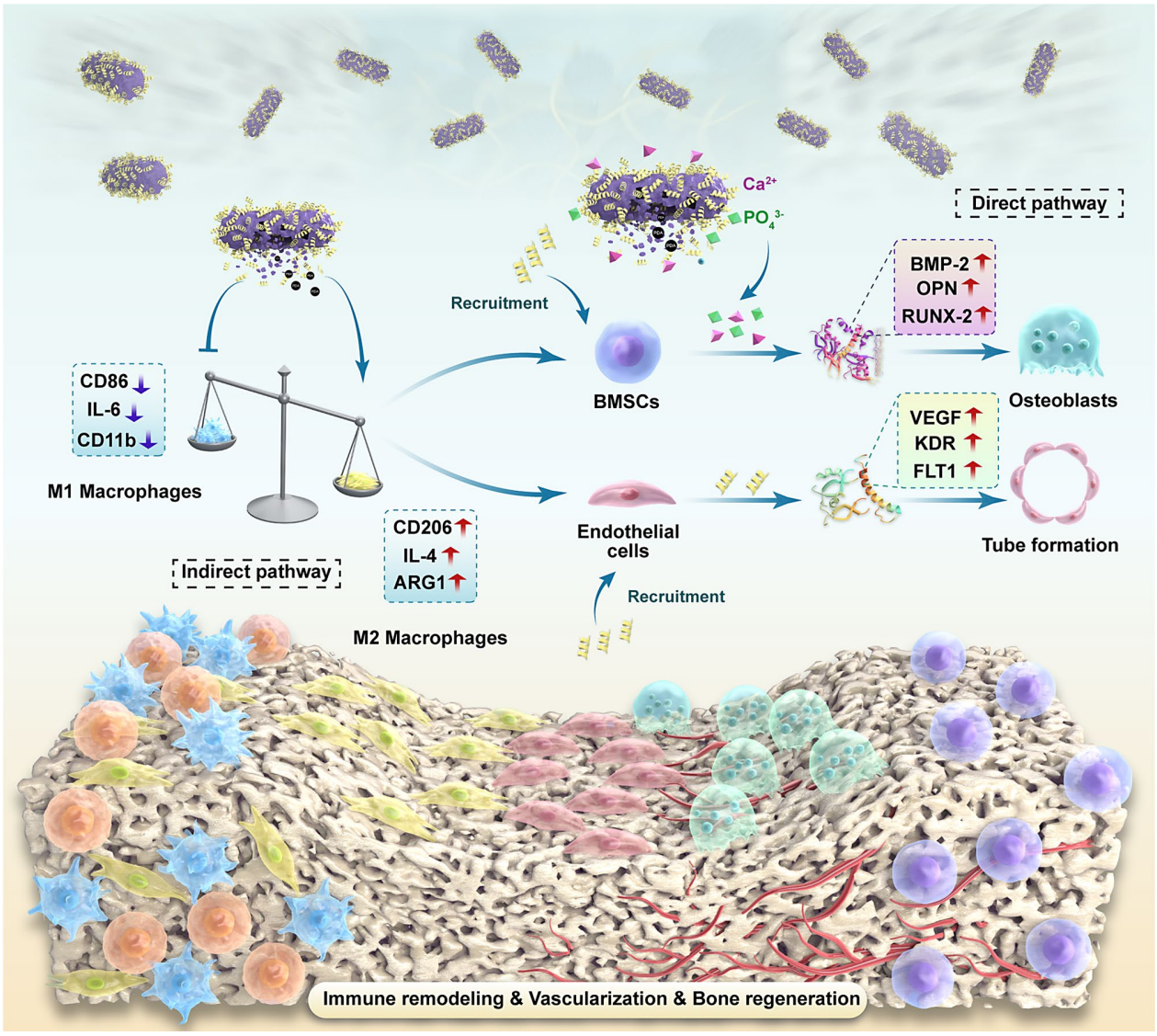

immune microenvironment for subsequent vascularized bone regeneration [2–5].

In terms of vascularization, vascular endothelial growth factor (VEGF) is one of the most important growth factors regulating vascular development and generation and plays an important role in bone defect repair [6]. However, VEGF has limited stability and is easily degraded in vivo. Peptides are regarded as powerful alternatives to growth factors because of their unique advantages [7]. For example, the QK peptide, a short peptide that mimics VEGF, can recruit vascular endothelial cells and promote angiogenesis and has unique advantages in hydrogel loading because of its small molecular weight and high stability [8]. In addition, QK peptides are involved in the remodelling of the local immune microenvironment while promoting tissue repair [9, 10]. Therefore, hydrogel scaffolds that can continuously deliver QK peptides may be excellent at improving the immune microenvironment and promoting vascularized bone regeneration [11].

The depletion of bone repair substances also limits bone repair. The bone repair process requires several osteoblasts and a bone matrix. However, these repair substances are often limited to bone defects, resulting in a slow or even failed repair process. Nanoscale tricalcium phosphate (TCP), a bioceramic material with an inorganic composition similar to human bone tissue, has good osteoconductivity and can effectively promote the regeneration of bone tissue [12]. Nevertheless, the rapid degradation rate of TCP does not match the rate of new bone formation, limiting its application in bone

repair. Dopamine (DA), which contains catechol functional groups and lysine-terminated amino functional groups, can form a homogeneous protective shell of polydopamine (PDA) on the surface of TCP via an oxidative polymerization reaction based on the protein adhesion mechanism of marine mussels [13]. This protective shell slows the degradation rate of TCP and promotes the deposition of calcium ions (Ca2+), thus potentially improving bone repair [14]. In addition, PDA has certain antioxidant properties, which can promote the polarization of macrophages to the M2 type and the secretion of anti-inflammatory and pro-healing cell growth factors, thus creating a more stable and favourable microenvironment for the bone repair process [15].

In this study, we innovatively designed a core–shell multifunctional nanoparticle (TPQ) that addresses three key challenges in bone repair through an organic–inorganic synergistic mechanism: anti-inflammatory regulation, angiogenesis, and osteogenic induction. Specifically, the molecular-level integration of the TCP inorganic phase and the PDA organic phase results in the formation of a biomimetic biphasic system. The TCP core not only provides a bone-like mineral matrix (osteoconductive) that serves as a biomimetic interface for cell adhesion but also promotes osteogenic differentiation through the continuous release of Ca2+/PO43- gradients (osteoinductive). The PDA shell achieves QK peptide loading and pH-responsive release through dynamic interface engineering to reshape the immune microenvironment and promote angiogenesis [16]. Therefore, TPQ nanoparticles have superior osteogenic performance over single-phase or mechanically blended materials because of their dual-phase reinforcement mechanism and immunometabolic crosstalk between released ions and peptides.

To address the clinical imperative of reconstructing geometrically complex bone defects, we engineered an injectable photocrosslinkable hydrogel (TPQGel) by integrating TPQ nanoparticles into a methacryloyl gelatin (GelMA) matrix (Scheme 1). This platform achieves phase therapeutic delivery through three interconnected biological cascades: (1) Inflammatory phase resolution: the antioxidant capacity of the PDA shell synergizes with pH-responsive QK peptide release to drive macrophage polarization toward the M2 phenotype, establishing an anti-inflammatory microenvironment while initiating angiogenic priming. (2) Proliferative phase activation: Sustained QK presentation induces osteoprogenitor cell homing and endothelial network formation through chemokine-mediated recruitment, enhancing defect-site cellularity. (3) Osteogenic phase reinforcement: progressive TCP degradation establishes Ca^{2+}/PO_4^{3-} gradients that synergize with macrophage-derived cytokines (IL-10, TGF-β) to promote matrix mineralization and osteoblast differentiation. Notably, the core constituents of the TPQ nanoparticles, namely, TCP and PDA, have secured FDA certification. In addition, the system innovatively employs QK peptides as a substitute for costly growth factors, thereby markedly reducing production costs and conferring substantial advantages in clinical translation.

Results and discussion

Preparation and characterization of composite hydrogels

First, PDA was synthesized via the oxidative polymerization of DA, and the TCP surface was modified and then loaded with QK peptides to form TPQ composite nanoparticles. The initial step in the synthesis process involves adding dopamine to a hydrochloric acid (HCl) solution. As time progressed, the color of the solution gradually darkened. After freeze-drying, the residual solid material was analyzed via transmission electron microscopy (TEM) and elemental distribution, and the results confirmed the successful synthesis of PDA. (Fig. 1A, S1). The TCP was then introduced into the PDA solution, where the oxidative polymerization reaction occurred under ultrasound, thus gradually forming TCP@PDA composite nanoparticles. TEM images revealed that TCP@PDA possessed a needle-like structure typical of calcium phosphate carriers, and its dispersed state formed a more compact structure (Fig. 1B). TPQ composite nanoparticles were then constructed by introducing QK peptides into the TCP@PDA composite nanosystems through noncovalent interaction mechanisms, including physical adsorption, hydrogen bonding, and electrostatic interactions. This was achieved because of the abundant functional groups on the surface of PDA, such as catechols, amine groups, and aromatic rings. Fourier transform infrared (FTIR) spectroscopy was used to verify the successful synthesis of the TPQ composite nanoparticles. The FTIR spectrum of pristine TCP revealed two characteristic absorption peaks at approximately 1031 cm^{-1} and 560 cm^{-1}, related to the stretching vibration of the O–P bond, thus confirming the existence of TCP. The FTIR spectra revealed new peaks at 1559 cm^{-1} and 1365 cm^{-1} (corresponding to the stretching vibration of C = C and the shear vibration of N–H, respectively) when PDA was modified, indicating successful polymerization of PDA. The absorption peaks of TPQ at 1662 cm^{-1}, 1550 cm^{-1}, and 1210 cm^{-1} were more significant than those of TCP@PDA, mainly because of the abundant amide bonds in the QK peptide, further confirming the successful construction of the TPQ nanoparticles (Fig. 1C, S2).

GelMA hydrogels are widely used in biomedical fields because of their excellent biocompatibility and injectable properties. This hydrogel was synthesized through chemical modification of gelatin by introducing reactive methacrylate (MA) groups, which endows the hydrogel with photosensitizing properties. FTIR analysis revealed

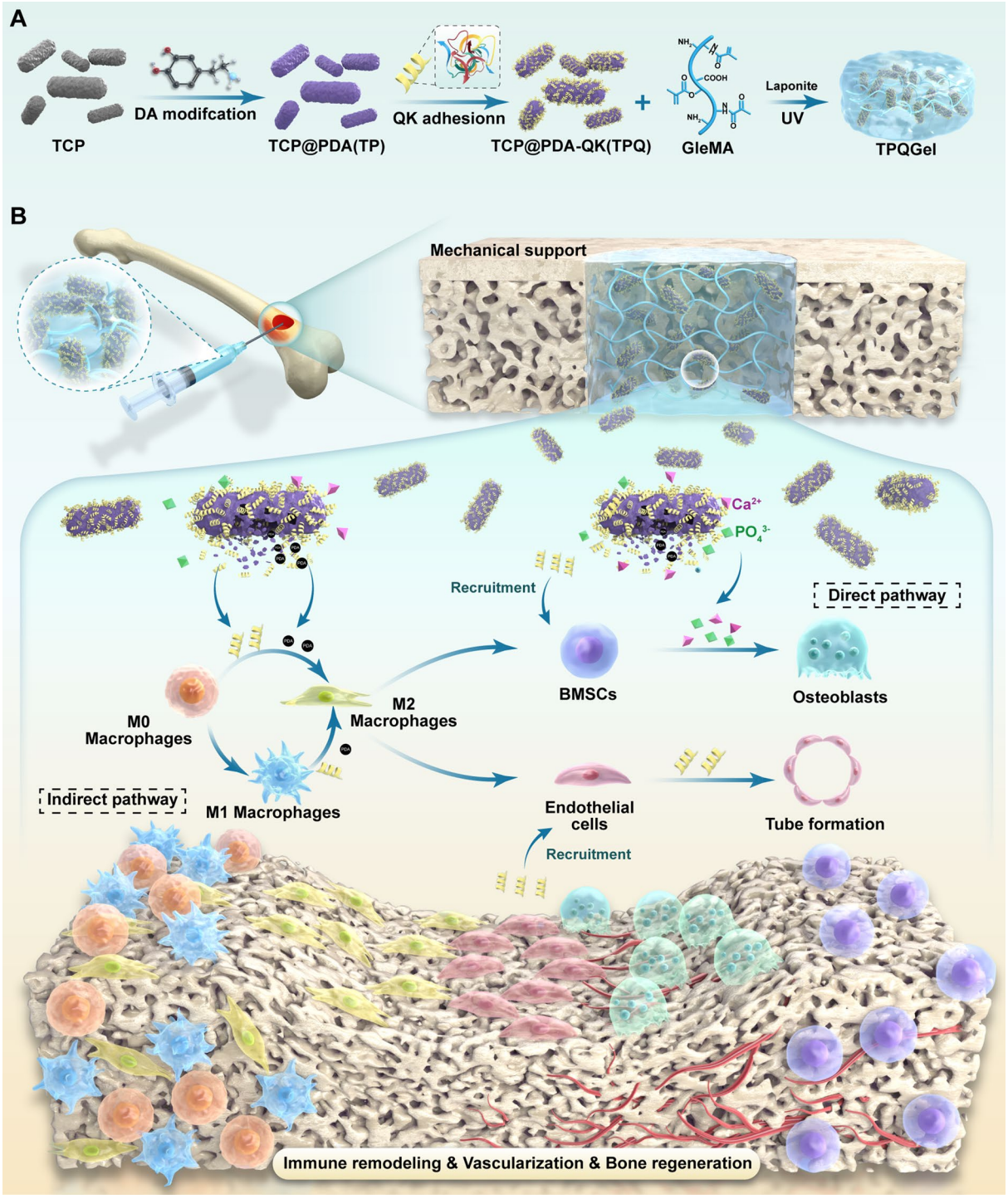

Scheme 1 Schematic representation of the synthesis of the TPQGel hydrogel and its therapeutic efficacy in treating bone defects. (**A**) Injectable TPQ-Gel hydrogel design and preparation. (**B**) The TPQGel hydrogel is capable of not only precisely filling bone defects but also progressively releasing TPQ nanoparticles. The outer shell layer of PDA on the TPQ nanoparticles, along with its incorporated QK peptide, can initially engage and modulate the M2 polarization of macrophages. This interaction leads to the secretion of various pro-healing growth factors, thereby indirectly fostering vascularized bone regeneration. Additionally, the sustained release of the QK peptide also plays a role in the recruitment of stem cells and other cellular components, increasing the cell density at the injury site and accelerating the vascularized bone regeneration process. The calcium and phosphorus mineral components that are released from the degradation of TCP within the core of the TPQ nanoparticles replenish the substances depleted during bone repair, further facilitating osteogenic differentiation. Through this dual mechanism of action, the TPQGel hydrogel has emerged as a promising therapeutic approach for the treatment of bone defects.

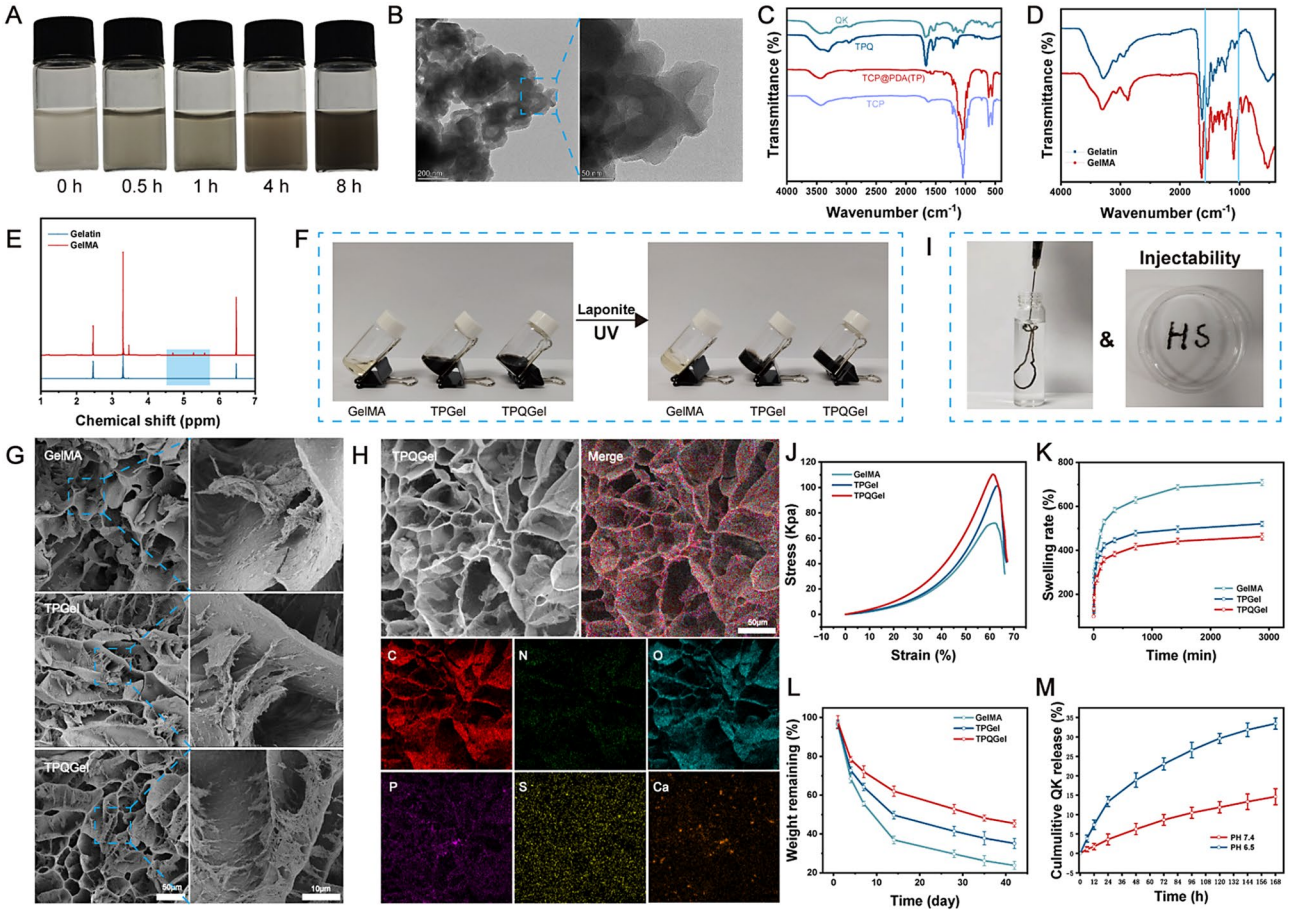

Fig. 1 Preparation and characterization of the TPQGel hydrogels. (**A**) Color change of the PDA solution. (**B**) TEM image of TCP@PDA. (**C**) FTIR spectra of TCP, TCP@PDA, TPQ, and QK. (**D**) FTIR spectra of GelMA and gelatin. (**E**) 1HNMR spectra of GelMA and gelatin. (**F**) Schematic diagram of the liquid–solid transition of the GelMA, TPGel, and TPQGel hydrogels. (**G**) SEM images of the GelMA, TPGel, and TPQGel hydrogels. (**H**) EDS image of the TPQGel hydrogel. (**J**) Stress–strain curves of the GelMA, TPGel, and TPQGel hydrogels. (**K**) Dissolution curves of the GelMA, TPGel, and TPQGel hydrogels. (**L**) Degradation curves of the GelMA, TPGel, and TPQGel hydrogels. (**M**) Release curves of the QK peptides from the TPQGel hydrogels

a key change in the synthesis of the GelMA hydrogel. Specifically, the C = O stretching vibration in the amide I band was redshifted to 1660 cm^{-1} compared with that of unmodified gelatin. This phenomenon is attributed to the overlap of the C = C stretching vibration signal of GA at 1695 cm^{-1} with the C = C stretching vibration signal of GA at 1695 cm^{-1} (Fig. 1D). The successful synthesis of the GelMA hydrogels was further confirmed via proton-1 nuclear magnetic resonance (1H NMR) spectroscopy, where the methyl (-CH = CH2) proton peaks at 5.46 ppm and 5.67 ppm indicated that the double bond had been successfully introduced into the gelatin, completing the synthesis of the GelMA hydrogels (Fig. 1E). The TP and TPQ nanoparticles were then introduced into the GelMA hydrogel system to form TPGel and TPQGel premixes, respectively. These premixes were transformed from a flowing solution to a stable gel state under irradiation with 405 nm UV light. This transformation was crucial for the formation of photocrosslinked hydrogels (Fig. 1F). Scanning electron microscopy (SEM) images revealed that the hydrogels had porous and fibrous structures, which increased the cell contact area and provided a favourable environment for cell growth (Fig. 1G). Energy dispersive X-ray spectroscopy (EDS) analysis revealed that C, N, O, P, S, and Ca were uniformly distributed in the TPQGel samples, further verifying the successful synthesis of the TPQGel hydrogels (Fig. 1H, S3). Notably, the TPQGel hydrogel also maintains excellent injectability and plasticity, thereby providing a broader scope for its clinical application. As clearly observable from the supplementary video, upon being injected through a syringe needle, the hydrogel can maintain a stable structure and shape, whether in a liquid medium or in air, demonstrating excellent mechanical stability. This feature endows it with unique advantages in clinical settings. In minimally invasive surgeries, surgeons can precisely deliver the hydrogel to the fracture site or bone defect area via injection. This approach circumvents the extensive tissue damage associated with traditional open surgeries, significantly reduces surgical risks, and

facilitates patients' postoperative recovery (Fig. 1I, Video 1). In addition to being injectable, the TPQGel hydrogel also exhibited excellent elasticity and stability. Even after repeated compression, the original shape of the composite hydrogel can be restored without obvious fracture or collapse (Video 2, Figure S4). Furthermore, in-depth analysis of the stress–strain curve indicated that although the introduction of TP and TPQ nanoparticles enhanced the mechanical properties of the hydrogel to a certain extent, their strengthening effect was still significantly different from that of natural cancellous bone (Fig. 1J). In the future, further optimizing the dispersity and interfacial interactions of nanoparticles will be the key to improving the mechanical properties of hydrogels. This can be achieved by precisely controlling the size, shape, and surface modification of nanoparticles [17].

In addition, the hydrogel samples were immersed in phosphate-buffered saline (PBS) at 37 °C to evaluate the swelling (within 48 h) and degradation properties (within 42 days) of the hydrogels. The hydrogels rapidly absorbed PBS during the initial 0–2 h of the experiment, resulting in a significant increase in weight, which stabilized after 25 h, indicating that swelling equilibrium had been reached. However, the incorporation of TP and TPQ effectively reduced the swelling rate and maintained the stability of the hydrogel structure, which can improve the repair process of bone tissues (Fig. 1K). The degradation test results revealed that the hydrogels gradually degraded over time. However, the degradation rates of the TPGel and TPQGel hydrogels were significantly lower than those of the GelMA hydrogels, suggesting that the composite hydrogels have longer-term stability, which is essential for long-term bone repair and regeneration (Fig. 1L). On the basis of the biomimetic strategy of the pathological microenvironment, we employed HEPES buffer (pH 7.4) to simulate normal bone tissue fluid and acetate buffer (pH 6.5) to simulate the inflammatory microenvironment. Through dynamic dialysis, the drug-controlled release behavior of the TPQGel was systematically evaluated. The results revealed that the TPQGel hydrogel exhibited a faster release rate and greater release amount under acidic conditions. This phenomenon is attributed primarily to the protonation of the catechol structure in PDA molecules in acidic environments, which weakens their interaction with drug molecules and thereby accelerates drug release. The pH-responsive characteristics of the TPQGel hydrogel enable it to precisely match the temporal and spatial demands of bone repair—the rapid release of the QK peptide during the inflammatory phase to reshape the immune microenvironment—thus laying the foundation for subsequent vascularized bone regeneration (Fig. 1M).

In summary, the TPQGel hydrogel possesses excellent injectability, superior biocompatibility, and pH-responsive drug release characteristics. These attributes render it highly promising for broad clinical applications, particularly in the minimally invasive treatment of bone defects.

In vitro biocompatibility assessment

The performance of scaffolds is critical for cell viability, adhesion, and proliferation in the field of bone tissue engineering. This performance can be reflected by evaluating the growth of MC-3T3-E1 cells and HUVECs. In this study, the cells were first cocultured in 96-well plates and observed at the critical time points of 1, 3, and 5 days. The results of the CCK-8 assay revealed that the proliferation levels of the cells in each group were not significantly different at the initial stage of culture (day 1). However, the level of cell proliferation was significantly greater in the TPQGel group than in the other groups at days 3 and 5. The Control group presented the lowest cell proliferation level at days 3 and 5. This result reveals that the TPQGel hydrogel provides a superior environment for cell proliferation because of its loaded TPQ nanoparticles (Fig. 2A and C). In addition, live/dead cell staining of the cocultured cells revealed that the MC-3T3-E1 cells with HUVECs exhibited high viability in the TPQGel, TPGel, and Control groups on day 3, with most of the cells displaying green fluorescence (representing live cells) and only a few displaying red fluorescence (representing dead cells). Moreover, the cell density was significantly greater in the TPQGel group than in the other two groups, which was consistent with previous results (Fig. 2B and D).

Recent studies have shown that cell morphology plays a crucial role in regulating the cellular phenotype [18]. Cytoskeletal staining revealed that MC-3T3-E1 cells exhibited a larger stretch area and typically elongated spindle morphology in the TPQGel group than in the Control and TPGel groups on day 3. This morphology was closely associated with the adhesion, proliferation, and differentiation of osteogenesis-associated cells (Fig. 2E). Further quantitative analysis revealed that the TPQGel group presented the highest cell density and stretch area (Fig. 2F and G). In addition, HUVECs revealed a similar trend, with the best stretch morphology and proliferation ability in the TPQGel group (Fig. 2H). The quantitative results revealed that the cells in the TPQGel group had greater density and a larger stretch area (Fig. 2I and J). These results indicate that the hydrogel environment in the TPQGel group is favourable for cell adhesion and proliferation, providing a superior scaffold option for bone tissue engineering.

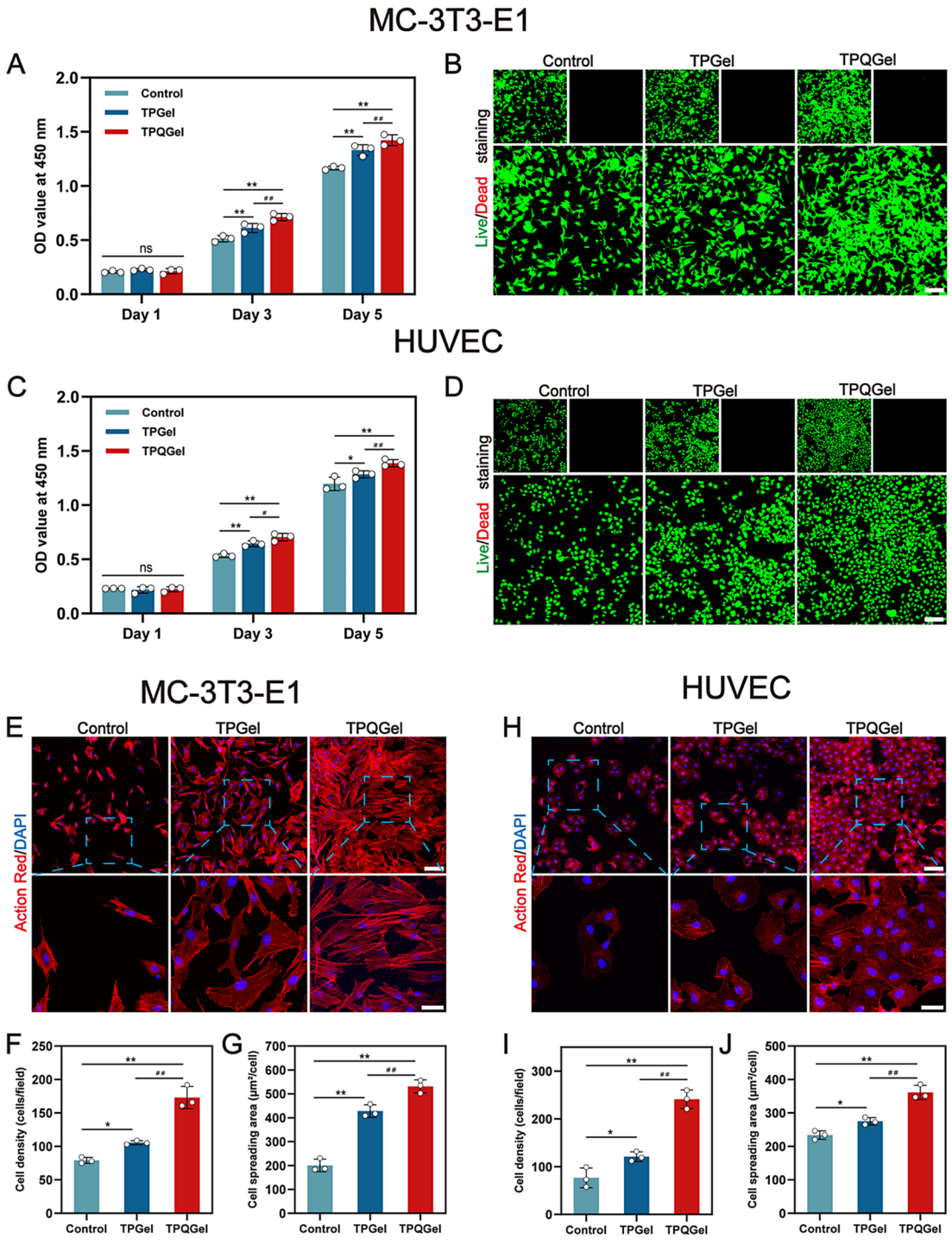

Fig. 2 In vitro biocompatibility analysis of the TPGel hydrogels and TPQGel hydrogels. (**A**) CCK8 assay and (**B**) live–dead staining of MC-3T3-E1 cells. (**C**) CCK8 assay and (**D**) live–dead staining of HUVECs. (**E**) Cytoskeletal fluorescence staining for F-actin and DAPI in MC-3T3-E1 cells and (**F**) HUVECs. Quantitative analysis of (**G**) the cell density and (**H**) the cell spreading area of MC-3T3-E1 cells. Quantification of (**I**) the cell density and (**J**) the cell spreading area of HUVECs. Scale bars: 100 μm (**B**, **D**), 50 μm (low-magnification images in **E**, **H**), and 20 μm (high-magnification images in **E**, **H**). The data are presented as the means ± SDs ($n = 3$). $^{*}p < 0.05$, $^{**}p < 0.01$ indicate significant differences compared with the Control group. $^{\#}p < 0.05$, $^{\#\#}p < 0.01$ indicate significant differences compared with the TPGel group

The TPQGel promoted M2-type macrophage polarization to remodel the immune microenvironment

Macrophages exhibit good plasticity in the complex microenvironment following bone injury [19]. Macrophages respond rapidly to the proinflammatory M1 type at the onset of injury, exacerbating the inflammatory response through the secretion of cytokines, such as tumor necrosis factor-α (TNF-α) and interleukin 6 (IL-6), thereby effectively removing damaged, dead cells and their debris. This stage is critical for preventing infection and subsequent repair processes [20]. As the inflammatory response gradually decreases, macrophages begin to shift to the M2 type, which has anti-inflammatory and prorepair properties. This shift is crucial for regulating the local immune microenvironment and promoting vascularization and bone regeneration [21]. M2 macrophages promote tissue repair through the secretion of anti-inflammatory cytokines (interleukin 4 (IL-4) and transforming growth factor β (TGF-β)) and angiogenic growth factor (VEGF), thus providing favourable conditions for tissue repair and regeneration [22].

In this study, the effects of the hybridized hydrogels on the activity of RAW264.7 macrophages were evaluated via a CCK-8 assay and live/dead staining. The results revealed that the number of macrophages in the TPGel and TPQGel groups gradually increased with increasing incubation time, whereas the number of dead cells was relatively low, indicating that the two hydrogels had good biocompatibility and could support macrophage survival and proliferation (Fig. 3A and B). A two-step treatment strategy was adopted to simulate the in vivo inflammatory environment and explore the effect of the composite hydrogels on macrophage polarization. First, the macrophages were prestimulated with lipopolysaccharide (LPS) to mimic the microenvironment at the beginning of inflammation. The prestimulated cells were then treated with different hydrogels or PBS to assess the effects of these materials on the direction of macrophage polarization. Compared with that in the Control group, the expression level of CD86, a marker of M1-type macrophages, was significantly greater in LPS-stimulated macrophages, whereas the expression of CD206, a marker of M2-type macrophages, was significantly lower, suggesting that LPS efficiently induced macrophage polarization toward the M1-type. LPS prestimulation gradually decreased the expression level of CD86 in the cells in the LPS + TPQGel and LPS + TPQGel groups but gradually increased CD206 expression, indicating that the hydrogels can regulate the polarization of macrophages from the M1 phenotype to the M2 phenotype. Notably, the M2-type polarization of macrophages was pronounced in the LPS + TPQGel group, indicating the ability of the TPQGel hydrogel to promote M1-type to M2-type macrophage polarization. Compared with that in the LPS group, the CD86 expression level was decreased in the LPS + TPGel group, whereas the CD206 expression level was increased, possibly because the PDA in the shell layer of the TP nanoparticles had certain antioxidant and anti-inflammatory effects (Fig. 3C and D). Immunofluorescence staining supported the results of flow cytometry. The CD86 fluorescence intensity gradually decreased in the LPS, LPS + TPGel, and LPS + TPQGel groups, whereas the CD206 fluorescence intensity gradually increased, further confirming that the TPQGel hydrogel plays a key role in promoting the transition of macrophages from the M1 type to the M2 type (Fig. 3E).

Moreover, the morphological changes in macrophages in the TPGel- and TPQGel-treated groups at the morphological level were assessed via cytoskeletal staining. The results revealed that the macrophages in the TPGel-treated and TPQGel-treated groups presented an elongated and flattened spindle morphology after LPS prestimulation. Moreover, the morphological features of the macrophages in the TPQGel-treated group were similar to the classical morphology of M2-type macrophages (Fig. 3F, S5). The expression of genes related to different phenotypes of macrophages in the Control, LPS, LPS + TPGel, and LPS + TPQGel groups at the molecular level was assessed via RT−qPCR. The results revealed that the expression levels of key genes, such as CD86, IL-6, and CD11b, were significantly greater in the M1-type macrophages of the LPS group than in those of the Control group. However, the expression levels of related genes, such as CD206, IL-4, and ARG-1, were significantly decreased in M2-type macrophages in the LPS group. Compared with that in the LPS group, the expression of genes related to M2-type macrophages was gradually upregulated in the LPS + TPQGel group, whereas the expression of genes related to M1-type macrophages was gradually downregulated (Fig. 3G). These findings provide strong evidence for the immunomodulatory function of TPQGel hydrogels at the molecular and cellular levels. In conclusion, the TPQGel promoted the establishment of an anti-inflammatory and reparative immune microenvironment by regulating the gene expression profile of macrophages, which is important for vascularization and bone regeneration.

In vitro evaluation of the TPQGel hydrogel for direct vascular regeneration

Studies have suggested that vascularization plays an important role in the process of bone regeneration. The formation of a neovascularization network is crucial for achieving effective bone repair [23]. Vascularization provides essential nutrients and oxygen to bone tissue and helps remove metabolic waste, promoting osteoblast metabolism and bone tissue formation [24]. Therefore, advanced functional biomaterials must possess strong

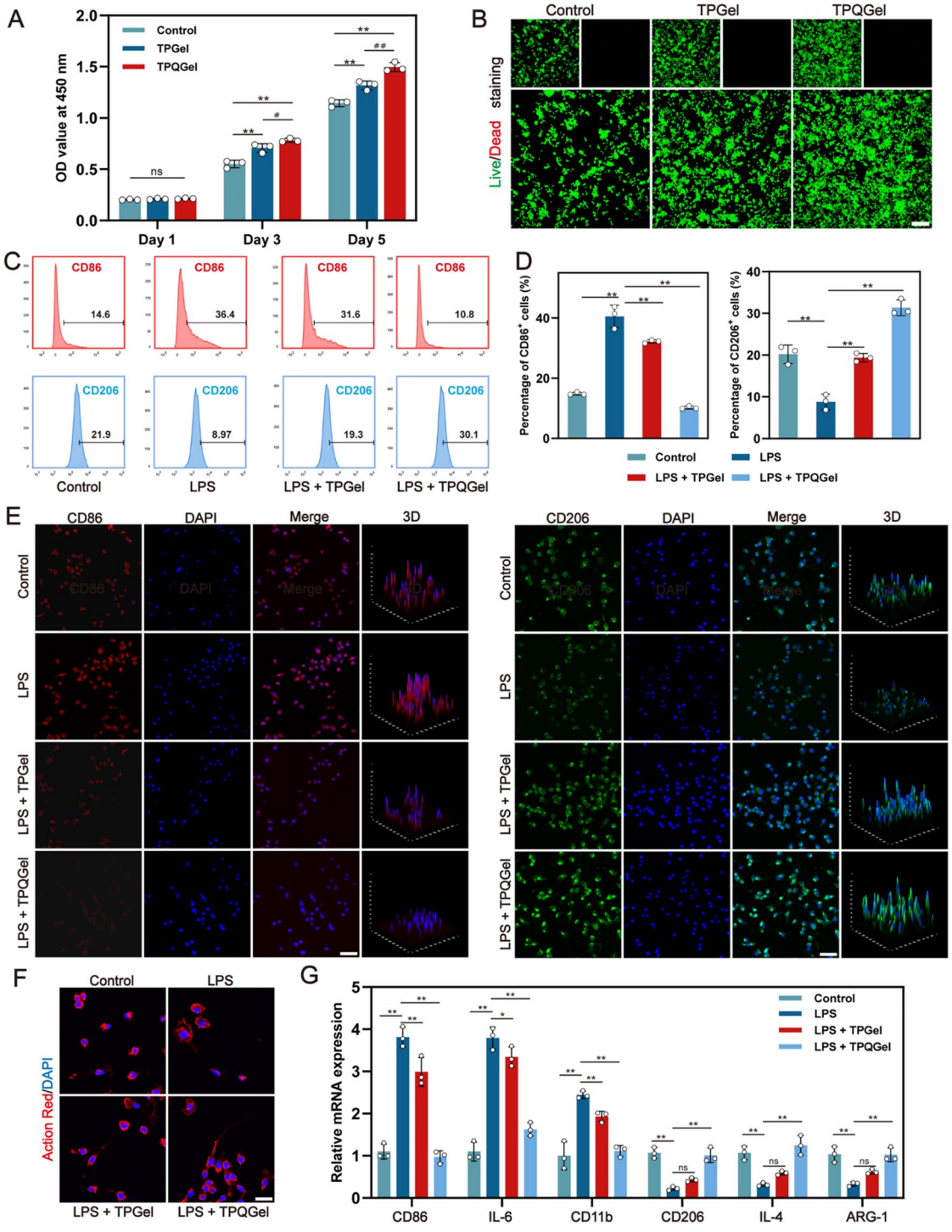

Fig. 3 TPQGel hydrogel-mediated reprogramming of macrophages. (**A**) CCK8 assay and (**B**) live–dead staining of RAW264.7 cells. (**C**) Flow cytometry analysis of CD86 and CD206 expression in RAW264.7 macrophages and (**D**) quantitative analysis. (**E**) Immunofluorescence staining of CD86 and CD206 in RAW264.7 macrophages. (**F**) Cytoskeletal fluorescence staining of F-actin and DAPI in RAW264.7 macrophages after different treatments. (**G**) Relative mRNA expression of inflammation-related genes in RAW264.7 macrophages. Scale bars: 100 μm (**B**), 20 μm (**E**), and 10 μm (**F**). The data are presented as the means ± SDs ($n = 3$). $^{*}p < 0.05$, $^{**}p < 0.01$ indicate significant differences compared with the Control group. $^{\#\#}p < 0.01$ indicates significant differences compared with the TPGel group

proangiogenic capabilities to meet the complex demands of bone healing [25].

In the present study, the effects of two hydrogels, TPGel and TPQGel, on the migratory ability of HUVECs were evaluated via wound healing experiments to evaluate the effects of composite hydrogel systems on angiogenesis. The results revealed that the TPQGel group had the fastest healing rate. The wounds in the TPQGel group were almost completely healed after 24 h, which was significantly better than the wounds in the TPGel group and Control group (Fig. 4A and C). This effect occurred mainly because of the sustained release of the QK peptide from the TPQ nanoparticles, which effectively promoted cell migration and angiogenesis. In addition, the cell recruitment ability of the TPGel and TPQGel hydrogels was assessed via Transwell experiments. The results revealed that the TPQGel group had the greatest number of transmembrane cells, which was approximately two and eight times greater than the number of transmembrane cells in the TPGel group and the Control group, respectively (Fig. 4B and D). These results suggest that the TPQGel hydrogel can significantly enhance the migration of HUVECs by releasing the QK peptide, which is essential for the vascularization of the bone defect region.

Furthermore, the pro-vascularization activity of the composite hydrogel was evaluated via an angiogenesis assay performed with Matrigel (Fig. 4E). The results were visible at 7 h. Specifically, significant tubular framework formation was detected in the TPGel and TPQGel groups, especially in the TPQGel group, where the tubular structure was more mature and complete with a greater density of cellular junctions (Fig. 4F). Quantitative analysis revealed that the TPQGel group had more nodes and a larger vascular area because of the cumulative effect of the continuous release of the QK peptide from TPQGel, leading to increased vessel formation (Fig. 4G and H). The rapidly established intact vascular meshwork promoted the transport of nutrients and related growth factors to the defect area, accelerating the bone repair process.

The QK peptide, a short peptide that mimics VEGF, effectively activates downstream signalling pathways, including the PI3K/Akt and MAPK pathways, by binding to VEGF receptors on the surface of vascular endothelial cells. These signalling pathways promote angiogenesis by increasing the expression of angiogenesis-related genes, such as VEGF, FLT1, and KDR [26]. In this study, the expression of these angiogenesis-related genes in HUVECs was evaluated via RT–qPCR. The results revealed that the expression levels of these genes were significantly greater in the TPQGel group than in the Control group (Fig. 4I). In addition, the protein expression of VEGF and CD31 in HUVECs was assessed via immunofluorescence staining. Fluorescence microscopy revealed that the fluorescence intensity of CD31 and VEGF gradually increased in the Control group, the TPGel group, and the TPQGel group after 3 days of coincubation, indicating increased vascularization (Fig. 4J). Quantitative analysis revealed that the fluorescence intensity was highest in the TPQGel group, which is consistent with the results of previous studies. These results demonstrate that TPQGel can accelerate the process of vascular regeneration by increasing the expression of genes and proteins related to angiogenesis (Fig. 4K).

In summary, the TPQ nanoparticles in the TPQGel hydrogel can gradually degrade and release QK peptides, recruit cells to reach designated sites, and increase the expression of angiogenesis-related genes and proteins, thus promoting vascularization and bone regeneration in the bone defect region.

In vitro evaluation of the ability of the TPQGel hydrogel to directly promote osteogenic differentiation

The initiation step of osteogenic differentiation is crucial for the bone regeneration process. This step involves the recruitment of osteogenic stem cells and other types of stem cells [27]. These cells migrate to the site of the bone defect after receiving specific chemical signals. The osteogenic stem cells then exhibit a remarkable proliferative capacity and initiate a series of complex differentiation programs to gradually transform into mature cells with osteogenic functions [28]. Effective cell recruitment ensures an adequate supply of osteogenic precursor cells and lays the foundation for the proliferation, differentiation, and osteogenic activity of these cells.

In this study, the ability of the composite hydrogel to recruit precursor osteoblasts was evaluated via wound healing experiments. The experimental results revealed that the wounds in the TPQGel group almost completely healed after 24 h. In addition, the cell migration rate was significantly greater in the TPQGel group (62%) than in the TPGel group (41%) and the Control group (28%), indicating that the TPQGel hydrogel can significantly promote cell migration (Fig. 5A and C). Transwell experiments further confirmed the recruitment effect of the TPQGel hydrogel. The experimental data revealed that the TPQGel group had the greatest number of transmembrane cells, which was approximately three and seven times greater than that of the TPGel group and Control group, respectively (Fig. 5B and D). These results suggest that the TPQGel hydrogel can promote the recruitment of precursor osteoblasts by gradually releasing the QK peptide.

Moreover, a cell coculture system was established via a Transwell device. Briefly, the hydrogels were placed in the upper chamber, and MC-3T3-E1 cells were placed in the lower chamber to evaluate the ability of the composite

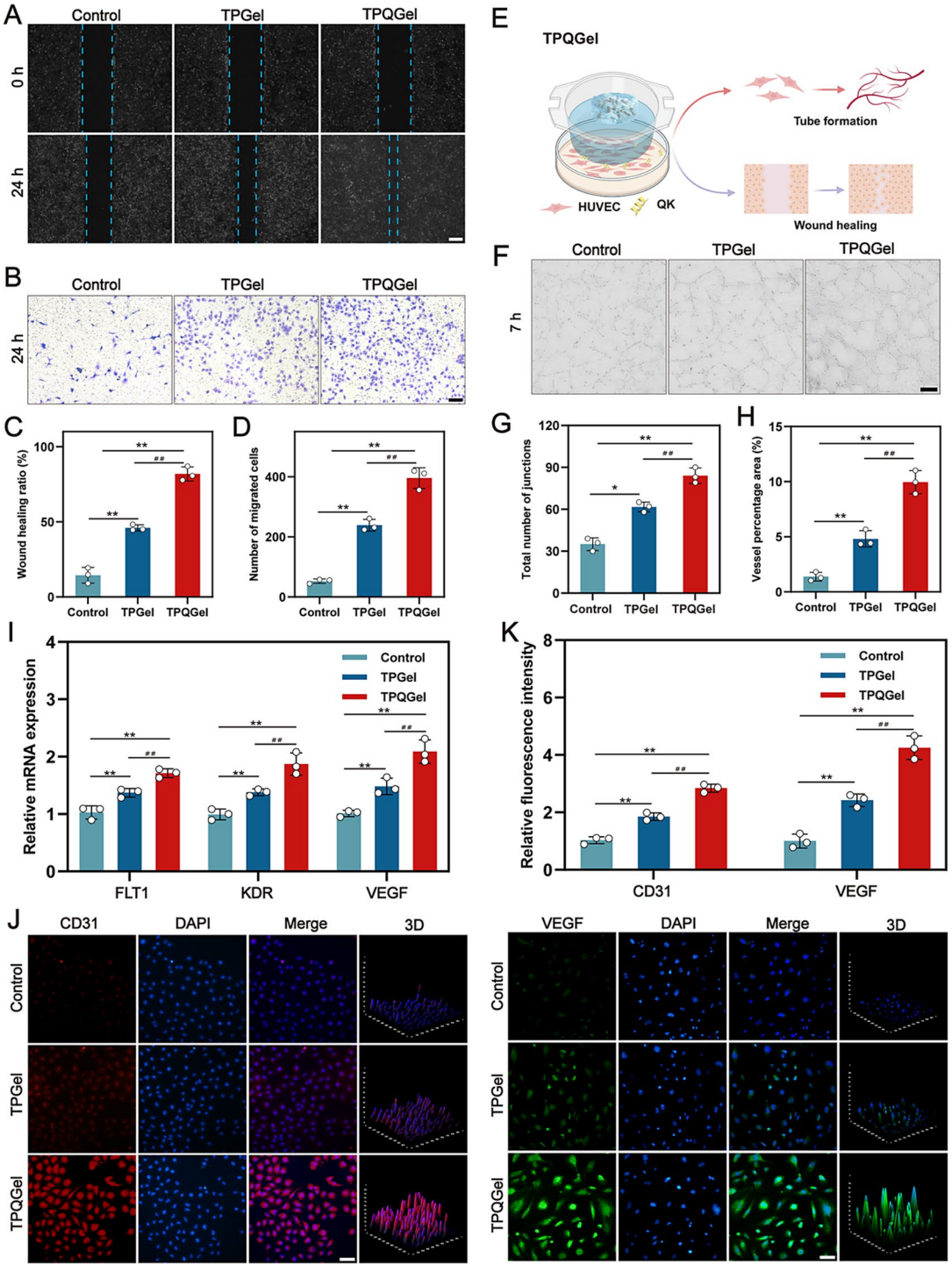

Fig. 4 The TPQGel hydrogel directly promoted angiogenesis. (**A**) Wound healing assay and (**B**) Transwell assay demonstrating the ability of the TPQGel hydrogel to promote cell migration and (**C**, **D**) quantitative analysis. (**E**) Schematic diagram of the effect of the TPQGel hydrogel on the angiogenic differentiation of HUVECs. (**F**) Vessel formation after different treatments and (**G**, **H**) quantitative analysis. (**I**) Relative mRNA expression of angiogenesis-related genes in HUVECs. (**J**) Immunofluorescence staining of CD31 and VEGF in HUVECs and (**K**) quantitative analysis. Scale bars: 200 μm (**A**, **F**), 100 μm (**B**), and 50 μm (**J**). The data are presented as the means ± SDs ($n = 3$). $^{*}p < 0.05$, $^{**}p < 0.01$ indicate significant differences compared with the Control group. $^{\#\#}p < 0.01$ indicates significant differences compared with the TPGel group

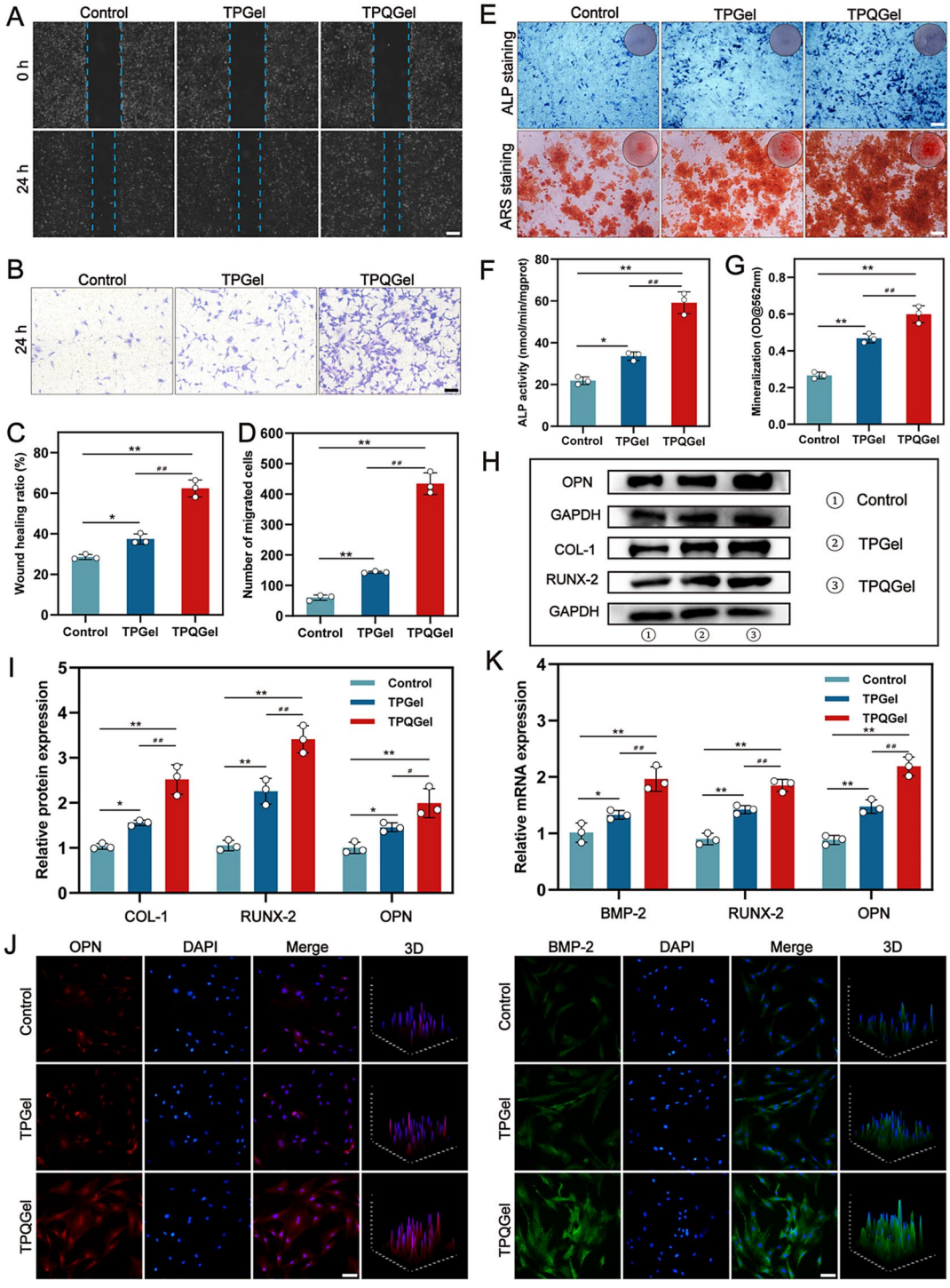

Fig. 5 The TPQGel hydrogel directly promoted osteogenic differentiation. (**A**) Wound healing assay and (**B**) Transwell assay demonstrating the ability of the TPQGel hydrogel to promote cell migration and (**C**, **D**) quantitative analysis. (**E**) Macroscopic and microscopy images of ALP staining and ARS staining of MC-3T3-E1 cells. (**F**) ALP activity and (**G**) quantitative analysis of ARS staining. (**H**) Western blot analysis of osteogenesis-related protein expression and (**I**) quantitative analysis. (**J**) Immunofluorescence staining of OPN and BMP-2 in MC-3T3-E1 cells. (**K**) RT–qPCR analysis of osteogenesis-related protein expression. Scale bars: 200 μm (**A**, **E**), 100 μm (**B**), and 50 μm (**J**). The data are presented as the means ± SDs ($n = 3$). $^{*}p < 0.05$, $^{**}p < 0.01$ indicate significant differences compared with the Control group. $^{\#}p < 0.05$, $^{\#\#}p < 0.01$ indicate significant differences compared with the TPGel group

hydrogels to contribute to osteogenic differentiation. Specifically, ALP expression was evaluated via alkaline phosphatase (ALP) staining after 7 days of coculture (early osteogenic differentiation). Quantitative analysis revealed that the TPQGel group presented the highest ALP activity, with more blue nodules and darker color in the optical and microscopy images, indicating high ALP activity. Calcium mineral deposition marks the beginning of the mineralization process of bone tissue at 21 days of coculture (late stage of osteogenic differentiation). The ability of the composite hydrogel to stimulate osteoblast mineralization was assessed via alizarin red S (ARS) staining. Macroscopic and microscopy images revealed that the TPQGel group presented the greatest number of bone mineralization nodules, with significantly increased positive staining (Fig. 5E and F). Quantitative analysis further confirmed the qualitative results of the ARS staining, providing accurate and reliable data to support the ability of the TPQGel hydrogels to induce osteoblast mineralization (Fig. 5G).

In addition, the regulatory effects of the composite hydrogels on osteogenesis-related proteins and gene expression were also evaluated. The key proteins involved in osteogenesis can be divided into two main categories: first, molecules that regulate osteoblast differentiation (transcription factors (RUNX-2) and bone morphogenetic proteins (BMP-2)). BMP-2 directs the differentiation of MC-3T3-E1 cells toward osteoblasts by activating the expression of a series of genes and precisely regulating the function of osteoblasts, which play a key role in bone formation and mineralization [29]. Second, the extracellular matrix proteins that constitute the main structural framework of bone tissues include osteoblastin (OPN), osteocalcin (OCN), and collagen type I (Col-I). These proteins provide necessary scaffolds for the mineralization process and participate in the regulation of key processes of osteoclasts, such as adherence, migration, and proliferation, through interactions with the cell surface receptor [30].

The effects of the hybridized hydrogels on the expression of osteogenesis-related proteins (Col-I, RUNX-2, and OPN) at the protein level were evaluated via Western blot experiments. The results revealed that the TPQGel group presented the highest expression levels of osteogenesis-related proteins (Fig. 5H and I). This may be related to the ability of the QK peptide to recruit osteoblasts and other stem cells, as well as the release of mineral components, such as calcium and phosphorus, from TCP degradation, further promoting osteogenic differentiation. In addition, the expression of osteogenesis-related proteins (RUNX-2, OPN, and BMP-2) was assessed via immunofluorescence. Fluorescence microscopy revealed that the fluorescence intensities of these proteins progressively increased in the Control group, the TPGel group, and the TPQGel group after 3 days of coincubation (Fig. 5J, S6). Quantitative analysis revealed that the TPQGel group presented the highest fluorescence intensity, further confirming the facilitating effect of the TPQGel hydrogel on the osteogenic process at the protein level (Fig. S7). A similar upregulation trend was detected at the gene level, with RUNX-2, OPN, and BMP-2 having the highest expression levels in the TPQGel group, followed by the TPGel group and the Control group (Fig. 5K). These results suggest that the TPQGel hydrogel can promote osteoblast recruitment, differentiation, and mineralization by gradually releasing QK peptides and mineral components, such as calcium and phosphorus.

Transcriptomic analysis of the mechanism by which TPQGel hydrogels influence macrophage reprogramming

A comprehensive RNA sequencing analysis was conducted to assess how TPQGel hydrogels promote macrophage polarization from the M1 to the M2 type. A statistical analysis of genes with more than 2-fold and statistically significant expression differences revealed significant differential expression of several genes in M2-type macrophages. Specifically, 1,314 genes were significantly upregulated, and 995 genes were significantly downregulated, indicating the complex network of gene regulation during polarization from the M1-type to the M2-type (Fig. 6A and B).

Through biological process analysis, the TPQGel hydrogel demonstrated multidimensional regulatory capabilities, with its molecular targets showing significant enrichment in critical pathways, including anti-inflammatory responses, osteogenic differentiation, and angiogenesis (Fig. 6C). These processes exhibit functional synergy during bone repair: the establishment of an anti-inflammatory microenvironment provides a foundation for tissue regeneration by modulating immune overactivation, while coordinated osteogenesis and angiogenesis promote structural remodelling and functional recovery in defect areas. KEGG pathway analysis revealed the involvement of TPQGel in the JAK-STAT, Toll-like receptor, and PI3K-AKT signalling pathways (Fig. 6D). Notably, the PI3K/AKT pathway is intricately associated with the polarization of macrophages toward the M2 phenotype. In the TPQGel hydrogel-treated group, genes characteristic of this pathway were upregulated. The network diagram clearly displays the interrelationships of key genes. (Fig. 6E and F).

To further investigate whether the TPQGel hydrogel mediates angiogenesis and bone regeneration by regulating the immune microenvironment, this study established a macrophage–hydrogel coculture system. After three days of coculture, the supernatant of each group of cells was collected for functional validation. The ability to

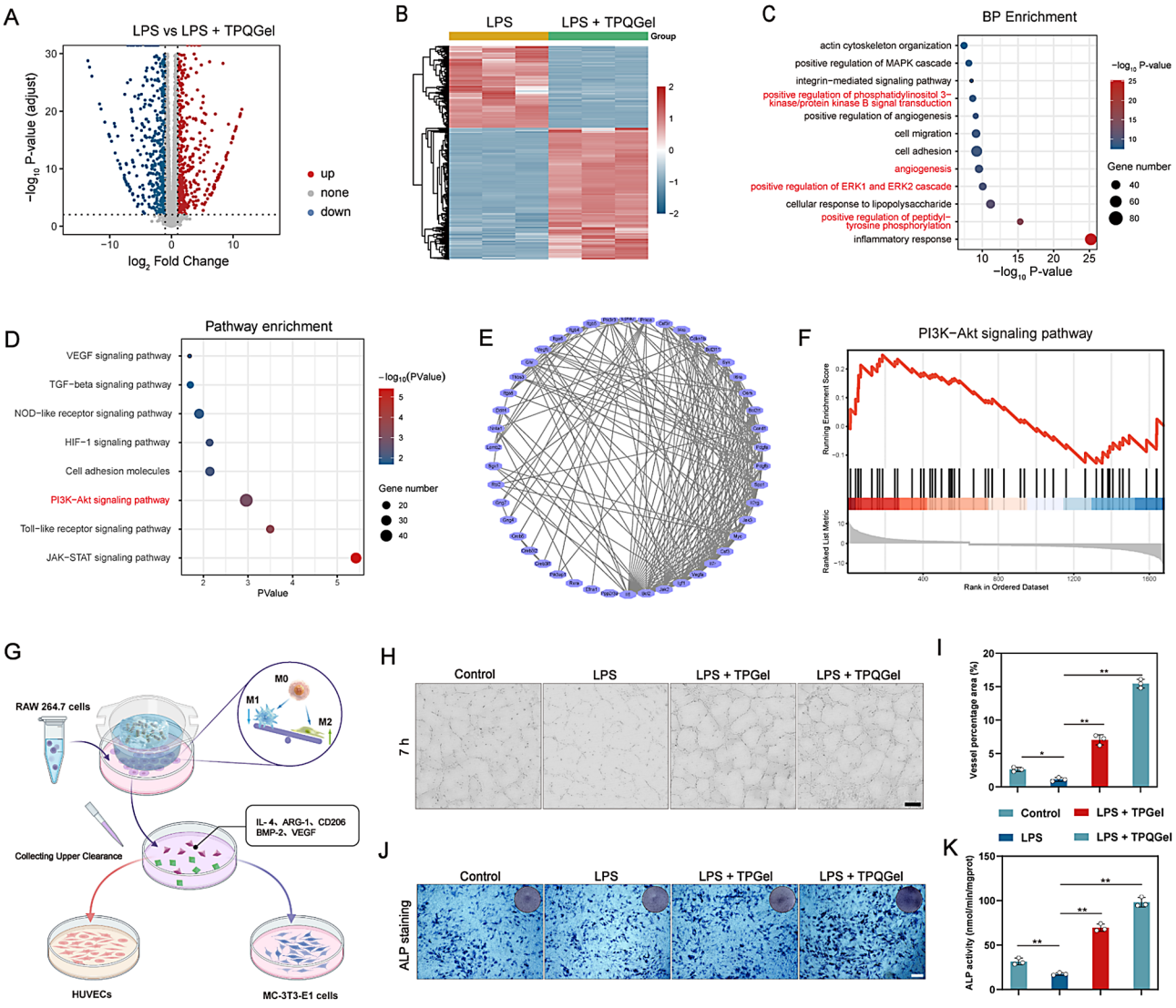

Fig. 6 Transcriptomic analysis of the mechanism of macrophage reprogramming by TPQGel hydrogels. (**A**) Volcano plots of the LPS group and the LPS + TPQGel group. Red represents upregulated genes, and blue represents downregulated genes. (**B**) Heatmap showing the overall gene expression levels in the LPS group and the LPS + TPQGel group. (**C**) Biological process (BP) and (**D**) KEGG analyses revealed potential pathways associated with the differentially expressed genes. (**E**) PI3K-AKT pathway gene relationship network map. (**F**) GSEA revealed that the number of genes enriched with the PI3K–AKT pathway significantly increased in the LPS + TPQGel group. (**G**) Schematic of the effects of supernatants from RAW264.7 macrophages subjected to different treatments on angiogenesis and osteogenesis. (**H**) Vessel formation after supernatant treatment and (**I**) quantitative analysis. (**J**) ALP staining and (**K**) quantitative analysis of MC-3T3-E1 cells after supernatant treatment. Scale bars: 200 μm (**H**, **J**). The data are presented as the means ± SDs ($n = 3$). $^{*}p < 0.05$, $^{**}p < 0.01$ indicate significant differences compared with the LPS group

promote angiogenesis was evaluated via the matrix colloid extracellular tube formation assay, and the osteogenic differentiation potential was analyzed via ALP staining and activity detection (Fig. 6G). In the context of angiogenesis, the supernatant of the Control group and the LPS group merely induced the formation of scattered microvascular fragments, and no obvious tubular structure formation was detected. In stark contrast, both the LPS + TPGel and the LPS + TPQGel groups demonstrated significant proangiogenic effects. Notably, the LPS + TPQGel group presented more mature vascular network characteristics: the lumen structure was continuous and intact, with endothelial cells tightly connected and forming multilevel branches (Fig. 6H and I). This dominant effect is likely ascribed to the TPQGel hydrogel synergistically promoting endothelial cell migration and lumen self-assembly by inducing M2 macrophages to secrete high levels of angiogenic factors, such as VEGF and PDGF-BB. A similar trend in osteogenic differentiation was also observed. The Control group presented typical blue mineralized nodules, whereas LPS stimulation led to a reduction in the number of nodules

and weakened staining intensity, indicating the inhibitory effect of the inflammatory microenvironment on osteogenic activity. Importantly, treatment with TPGel or TPQGel effectively reversed this phenomenon. The density of mineralized nodules in the LPS + TPQGel group not only gradually increased but also significantly increased ALP activity (Fig. 6J and K). By integrating these data with the early-stage polarization data of M2 macrophages, we postulate that this effect may be associated with the anti-inflammatory factors (such as IL-10 and TGF-β) and regeneration-promoting factors (such as BMP-2 and IGF-1) secreted by the TPQGel hydrogel through the induction of M2 macrophages.

Notably, the supernatant of macrophages cocultured with the hydrogel had more significant biological activity than did the hydrogel directly cocultured with osteoblasts and vascular endothelial cells. The supernatant promoted the formation of a more complete vascular network by vascular endothelial cells and enhanced the ALP activity of osteoblasts. This occurred because the drug released from the TPQGel reprogrammed the macrophages and promoted the secretion of a series of cytokines related to the promotion of angiogenesis and osteogenic differentiation, thus exerting additional pro-vascularization and bone regeneration effects (Fig. 4F, 5E and 6H and J).

Taken together, these findings indicate that TPQGel promoted the conversion of M1-type macrophages to M2-type macrophages and attenuated the inflammatory response, thereby indirectly promoting vascularization and bone regeneration.

In vivo evaluation of the early Immunomodulatory and vascular regenerative capacities of TPQGel hydrogels

Critical-sized bone defect models (diameter = 5 mm) were established in the left femur of Sprague–Dawley (SD) rats via surgical operation to explore the in vivo effects of TPQGel hydrogels. The defects were filled with drug-loaded TPQGel and TPQGel hydrogels to mimic the process of bone defect repair in clinical treatment (Fig. 7A and B).

In the initial stages of bone defects, inflammatory reactions occur most rapidly. The polarization direction of immune cells, particularly macrophages, is pivotal in determining the outcome of bone healing. Thus, we chose CD86 and CD206 as phenotypic markers for M1 and M2 macrophages, respectively, to assess the early-stage immune regulation of these hydrogel-based drug-loading platforms on bone defects. During the first week posttreatment, the immunohistochemical staining results revealed that the Control group presented the highest expression level of CD86 and the lowest expression level of CD206, suggesting that the bone tissue was in an inflammatory state. Comparatively, in the TPGel-treated and TPQGel-treated groups, we observed a progressive decrease in the expression of CD86, accompanied by a gradual increase in the expression of CD206, indicating attenuation of the inflammatory state (Fig. 7C). Notably, in the TPQGel group, the expression level of CD206 was the highest, whereas that of CD86 was the lowest (Figure S8). These findings demonstrate that the TPQGel hydrogel has the potential to modulate the early-stage transformation of macrophages from the proinflammatory M1 phenotype to the anti-inflammatory M2 phenotype. This modulation is highly important for reducing the inflammatory response and promoting bone repair.

In addition, the anti-inflammatory immune microenvironment created by TPQGel provides favourable conditions for vascular regeneration. M2-type macrophages can promote the release of VEGF, which promotes angiogenesis [31]. In terms of angiogenesis, we selected CD31 and VEGF as phenotype markers for HUVECs, and at the third week after treatment, we studied the effects of different treatments on angiogenesis through immunohistochemical staining. The results revealed that the expression levels of CD31 and VEGF were low in the Control group, indicating that the expression of genes related to vascular regeneration is inactive in the absence of exogenous stimulation, thus limiting vascular regeneration. However, the composite hydrogels gradually increased the expression of CD31 and VEGF, especially in the TPQGel hydrogel (Fig. 7D). Quantitative analysis further confirmed that the expression levels of CD31 and VEGF were the highest in the TPQGel group. These outcomes can be attributed to the positive facilitation of angiogenesis by the release of the QK peptide during degradation of the TPQGel hydrogel. Additionally, the presence of an anti-inflammatory and healing-promoting immune microenvironment, which is jointly created by the QK peptide and PDA, also contributed to these results (Fig. Fig. S9).

The hydrogel samples were subcutaneously embedded in SD rats to assess the degree of neovascularization. Naked-eye observation revealed limited blood vessel formation in the TPGel group. However, vascular network formation was visible in the TPQGel group, indicating abundant vascular infiltration (Fig. 7E). Further quantitative analysis revealed that the number of blood vessels was significantly greater in the TPQGel group than in the TPGel group and increased with time; this result is highly consistent with the characteristics of the TPQGel hydrogel (Fig. 7F). In the early stage, the TPQGel hydrogel can rapidly degrade and release the QK peptide and PDA. The QK peptide, which contains key sequences for cell adhesion and proliferation, effectively stimulates the proliferation and migration of vascular endothelial cells, thereby accelerating blood vessel formation. Owing to its unique physicochemical properties, PDA regulates the immune microenvironment, establishing a favourable

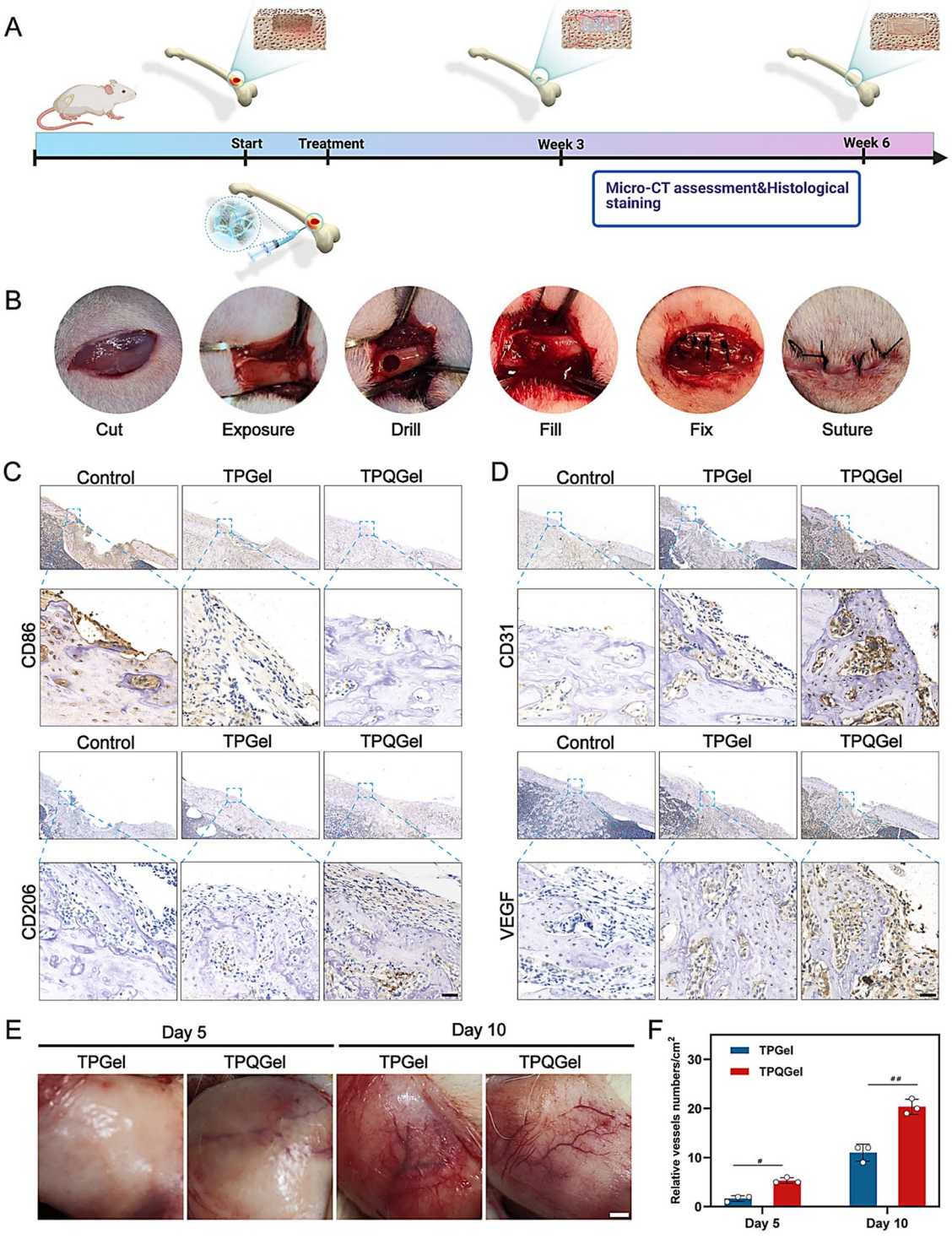

Fig. 7 Analysis of the in vivo immunomodulation and vascular regeneration capacity of the TPQGel hydrogel. (**A**) (**B**) Construction of the bone defect model and surgical procedure. (**C**) Immunohistochemical staining of CD86 and CD206 expression. (**D**) Immunohistochemical stainin of CD31 and VEGF expression. (**E**) Angiogenic images of the dorsal subcutis of rats on days 5 and 10 after hydrogel injection and (**F**) quantitative analysis. Scale bar: 5 mm (**E**), 30 μm (**C**, **D**). The data are presented as the means ± SDs ($n = 3$). $^{\#}p < 0.05$, $^{\#\#}p < 0.01$ indicates significant differences compared with the TPGel group

milieu for angiogenesis. These two components act synergistically to promote the abundant generation of blood vessels.

In vivo evaluation of the osteogenic differentiation capacity and biocompatibility of the TPQGel hydrogels

To assess the non-self-healing properties of critical-sized bone defects and the osteogenic efficacy of the composite implants, excised bone samples were analyzed via three-dimensional (3D) micro-CT reconstruction at postoperative intervals of 3 and 6 weeks. The results revealed that only a small amount of new bone was distributed at the edge of the defect area in the Control group at the 3rd postoperative week. In addition, significant bone defects were observed in the Control group at the 6th postoperative week, indicating that it is difficult to achieve self-healing of bone defects without external intervention. In contrast, new bone formation gradually increased in the TPGel group. In the TPQGel group, the bone defects were almost completely healed by the 6th week after surgery. This could be because the QK peptide and PDA can remodel the local immune microenvironment of bone defects, laying a solid foundation for the reconstruction of vascularization and the formation of bone tissues. The QK peptide can also recruit osteoblastic stem cells and other stem cells into bone defects. Furthermore, the QK peptide promoted the formation of blood vessels in the defect areas, thus promoting vascularized osteogenesis (Fig. 8A). The 3D reconstructed micro-CT images revealed that the bone regeneration indices, including the bone tissue volume to total tissue volume (BV/TV) ratio and trabecular thickness (Tb.Th), were consistent with the trend of the micro-CT images. The TPQGel group presented the highest values for the bone regeneration indices, indicating that this group had the most significant effect on bone regeneration (Fig. 8B and C). These results confirm the observations from the micro-CT images and provide precise numerical support, further confirming the remarkable ability of the TPQGel hydrogel to promote bone healing and regeneration.

The histopathological structure of the newborn bone tissue near the drilled hole was assessed via hematoxylin–eosin (H&E) staining. The results revealed that the defect area in the Control group was mainly composed of fibrous tissue at postoperative week 3, indicating that the natural healing ability of bone tissue is limited without the intervention of exogenous biomaterials. In contrast, significant bone trabecular deposition was detected in the TPGel and TPQGel groups. Compared with the TPGel group, the TPQGel group presented a more complete trabecular structure and greater potential for bone tissue regeneration. Although the number of bone trabeculae was not significantly different between the two groups at the 6th postoperative week, the TPQGel group revealed denser trabecular sorting and better tissue continuity than did the TPGel group (Fig. 8D and E). These results suggest that the TPQGel hydrogel can effectively promote the formation of bone trabeculae and improve the trabecular arrangement and structure, which is essential for achieving functional recovery of the bone defect area. In addition, immunohistochemical staining revealed that the expression of BMP-2 and OPN was significantly greater in the TPQGel group than in the other two groups at 3 weeks after surgery, which is consistent with the results of the quantitative analysis. These findings indicate that the TPQGel hydrogel is crucial in the process of bone regeneration and remodelling, especially in promoting matrix maturation and mineralization (Fig. 8F and G).

Furthermore, to assess the long-term in vivo biocompatibility of the composite hydrogel, it was injected into the femurs of normal Sprague–Dawley (SD) rats, and continuous observation was carried out for 12 weeks. The hearts, livers, spleens, lungs, and kidneys of the SD rats were subsequently collected for hematoxylin and eosin (H&E) staining. The results demonstrated that the tissue structure of each organ was intact, the cell morphology was normal, and there were no typical toxic-reaction characteristics, such as inflammatory cell infiltration and tissue necrosis. These findings indicate that the hydrogel and its degradation products (QK peptide, PDA, and TCP) do not cause toxic damage to important organs in vivo (Fig. 8H). To further evaluate the safety of the composite materials in the blood environment, a hemolysis experiment was conducted. After red blood cells (RBCs) were incubated with the TPGel and TPQGel hydrogels at different concentrations for 30 min, the absorbance of the supernatant was accurately detected via a spectrophotometer. The results revealed that the red blood cells in each experimental group remained intact, and there was no significant change in absorbance due to hemoglobin release. These findings fully indicate that the hydrogel has good stability and safety in the blood environment and does not cause adverse effects on the blood system (Fig. 8I). On the basis of the abovementioned experimental results of in vivo toxicity tests of important organs, blood compatibility, and in vitro cytocompatibility, it can be reasonably inferred that the degradation products of the TPQGel hydrogel have no obvious toxicity under the conditions used in this study or during the observation period. This conclusion provides crucial safety assurances for its subsequent clinical application in bone tissue repair.

Conclusion

The TPQGel hydrogel system developed in this study represents a comprehensive breakthrough from the material structure to the functional mechanism through

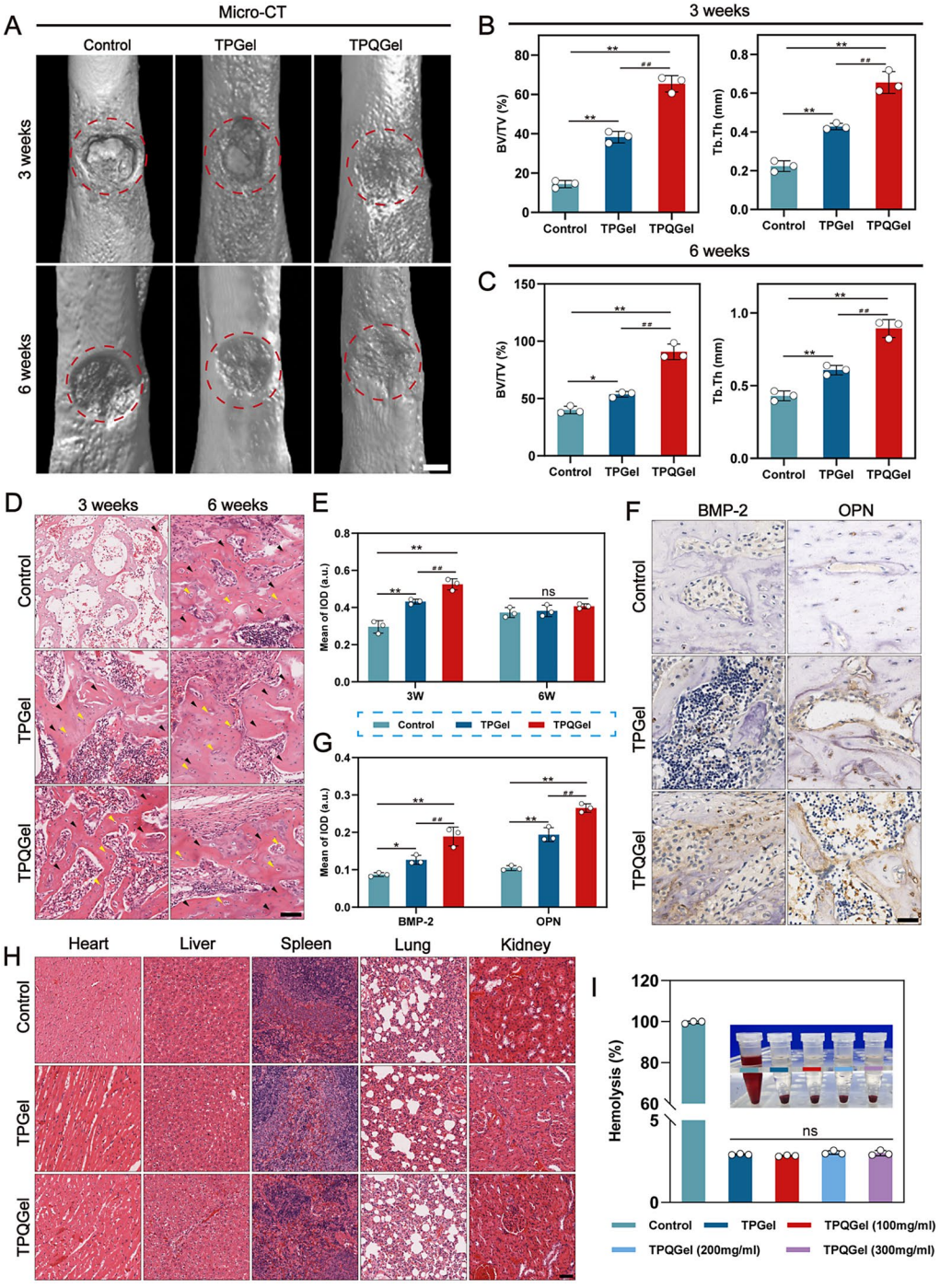

Fig. 8 In vivo osteogenic differentiation capacity and biocompatibility analysis of the TPQGel hydrogels. (**A**) Representative micro-CT images of SD rat femurs and (**B**, **C**) quantitative analysis. Images were taken at week 3 and week 6 after treatment. (**D**) HE staining and (**E**) quantitative analysis at weeks 3 and 6 after treatment (black arrow: newly formed bone trabeculae. Yellow arrow: The central tube of the newborn. Arrows are only used to indicate anatomical structures and do not represent significant differences.) (**F**) Immunohistochemical staining of BMP-2 and OPN at week 3 after treatment and (**G**) quantitative analysis. (**H**) HE staining of the heart, liver, spleen, lung and kidney. (**I**) Hydrogel hemolysis assay. Scale bars: 2 mm (**A**), 100 μm (**H**), and 30 μm (**D**, **F**). The data are presented as the means ± SDs ($n = 3$). $^{*}p < 0.05$, $^{**}p < 0.01$ indicate significant differences compared with the Control group. $^{\#\#}p < 0.01$ indicates significant differences compared with the TPGel group

an innovative multidimensional design. Its core innovation lies in the construction of a dynamically responsive organic–inorganic hybrid system, integrating core–shell TPQ nanoparticles (TCP–PDA–QK) into a photocurable GelMA hydrogel network through bionic interface engineering to form an intelligent Control platform. First, the core–shell structure design enables precise spatiotemporal drug delivery. The PDA shell endows the material with pH-responsive properties, significantly increasing the release efficiency of the QK peptide in the inflammatory microenvironment (pH 6.5). This enhances M2 polarization of macrophages and early vascular network reconstruction. The continuous release of mineral components such as calcium and phosphorus by the TCP core further promotes osteogenic differentiation, coupling immune regulation, angiogenesis, and osteogenic differentiation. Second, the organic–inorganic hybrid design facilitates the dynamic evolution of mechanical properties. As TCP degrades and mineral components such as calcium and phosphorus gradually deposit, the mechanical properties of newly formed bone progressively increase. Clinically, the photocuring and injectable properties of GelMA hydrogels enable minimally invasive filling of bone defects, overcoming the morphological limitations of traditional ceramic and metal implants. The incorporation of the QK peptide eliminates the need for expensive cytokines and cell-based therapies, significantly reducing production costs. Moreover, TCP and PDA comply with FDA standards, ensuring safety and effectiveness. Thus, the TPQGel hydrogel holds great promise as a novel scaffold material for treating bone defects.

Nevertheless, this study has several limitations. First, the in vitro and in vivo models primarily recapitulate bone repair under acute inflammatory conditions. However, impaired fracture healing frequently arises from a dysregulated transition to chronic inflammation or persistent pathological stimuli [32]. Future investigations should evaluate the efficacy of the TPQGel in chronic inflammatory microenvironments, such as diabetic or aged bone defects, to better align with clinical scenarios of delayed union [33, 34]. Second, while immune reprogramming has been identified as a central mechanism for vascularized osteogenesis, the potential effects of TPQGel on other immune populations (e.g., neutrophils, T cells, and dendritic cells) remain unexplored [35]. Targeted modulation strategies, such as macrophage-specific exosome delivery or CRISPR-edited cytokine release systems, could further dissect cell-type contributions [36, 37]. Finally, clinical translation faces three challenges: (1) the mechanical properties of the TPQGel hydrogel are limited, and its application in load-bearing parts needs further strengthening; (2) the long-term stability and pharmacokinetics of the QK peptide in vivo are undefined; [38] and (3) batch-to-batch variability during scaled hydrogel production is limited. Addressing these barriers will require material innovations (e.g., near-infrared-triggered gelation) coupled with rigorous pharmacodynamic profiling [39, 40].

Materials and methods

Materials

Gelatin was purchased from Sigma–Aldrich (Shanghai, China). Methacrylate (MA) was purchased from Andromax (Shanghai, China). QK peptide (KLTWQELYQLKYKGI, 99% pure) was purchased from Shanghai Qiangyao Biotechnology Co. TCP was purchased from Jiangsu Xianfeng Nanomaterials Science Co. DA, aminomethane (Tris), and lipopolysaccharide (LPS) were purchased from Sigma–Aldrich Trading Co., Ltd. (Shanghai, China). Fetal bovine serum (FBS), Dulbecco's modified Eagle's medium (DMEM), and alpha-modified Eagle's medium (α-MEM) were used. Purchased from Gibco Life Technologies Co. (Grand Island, USA). Endothelial cell medium was purchased from ScienCell Research Laboratories (Shanghai, China). The Cell Counting Kit-8 (CCK-8) and Live/Dead Staining Kit were purchased from Dojindo Laboratories (Kumamoto, Japan).

Preparation of the TPQ nanocomposites

The TCP nanoparticles were uniformly dispersed in a dopamine (DA) solution (2 mg/mL) through 30 min ultrasonication. Subsequently, the homogeneous suspension underwent continuous stirring at 60 °C for 12 h to promote oxidative polymerization of DA, resulting in the formation of a polydopamine (PDA) coating on the nanoparticle surface. The obtained TCP@PDA composite nanoparticles were harvested through centrifugation (10,000 rpm, 15 min) followed by vacuum drying. These particles were then reconstituted in deionized water (1 mg/mL) and functionalized with QK peptide through dropwise addition of peptide solution (1 mg/mL) under ambient conditions (25 °C) with 12 h magnetic stirring. Ultimately, the TPQ nanocomposites were collected via lyophilization (-50 °C, 0.1 mbar) for subsequent characterization.

Calculation of QK peptide modification efficiency

(1) Preparation of the TP solution: Fifty milligrams of TP nanoparticles were dissolved in 25 ml of enzyme-free water, and the mixture was sonicated and stirred for 0.5 h to obtain the TP solution.

(2) For the dissolution of the QK peptide, 50 mg of the QK peptide was dissolved in the aforementioned solution, and the mixture was stirred for 12 h.

(3) Measurement of unbound QK peptide: The amount of unbound QK peptide in the supernatant was determined via a BCA quantitative assay.

1) Construction of the QK standard curve.

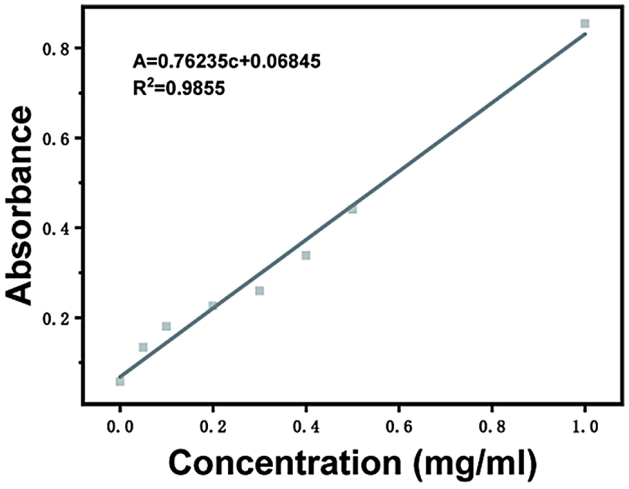

2) Measurement of the QK peptide content in the supernatant: The absorbance of the supernatant was measured three times, yielding values of 0.2244, 0.2805, and 0.2432, corresponding to QK peptide contents of 5.11 mg, 6.95 mg, and 5.73 mg, respectively.

(4) Calculation of the amount of bound QK peptide: The amount of bound QK peptide was calculated as the initial amount of QK peptide minus the amount of unbound QK peptide. From three independent experiments, the measured amounts of bound QK peptide were 44.89 mg, 43.04 mg, and 44.26 mg.

(5) Calculation of modification efficiency: The modification efficiency (%) was calculated as (bound QK peptide amount/initial QK peptide amount)×100%. In summary, the loading efficiencies of the QK peptide were 89.78%, 86.08%, and 88.52%, indicating that the method is stable and reliable.

Porous GelMA hydrogel preparation

(1) Fabrication of Methacrylated Gelatin (GelMA) Hydrogels: Gelatin type A was dissolved in phosphate-buffered saline (PBS, pH 7.4) under magnetic stirring (600 rpm, 50 °C) to obtain a 10% (w/v) homogeneous solution. Methacrylic anhydride (MA) was introduced via precision syringe pump infusion (0.5 mL/min) into the gelatin solution maintained at 37 °C in a thermostatic oil bath. Following 3 h methacrylation, the reaction was terminated through PBS dilution (1:5 v/v). Unbound MA molecules were eliminated via sequential centrifugation (5,000 ×g, 15 min) and PBS dialysis (MWCO 12–14 kDa, 38 °C, 48 h). The purified GelMA solution was lyophilized (-80 °C, 0.05 mbar) to yield a stable porous matrix.

(2) Engineering of Macroporous GelMA Scaffolds: For pore architecture control, GelMA (10% w/v) was blended with 2-hydroxy-4'-(2-hydroxyethoxy)-2-methylpropiophenone (I2959, 0.5% w/v) as photoinitiator. This prepolymer solution was emulsified with poly (ethylene oxide) (PEO, 20% w/v) aqueous solution (1:3 v/v) using high-shear homogenization (10,000 rpm, 5 min). The biphasic system underwent UV crosslinking (365 nm, 10 mW/cm², 5 min) to solidify the continuous GelMA phase. Subsequent PEO leaching was achieved through 24 h dialysis in DMEM medium (37 °C, 100 rpm), generating interconnected macropores (150–300 μm) essential for cellular ingression and metabolic exchange.

TPQGel in vitro administration

(1) Preparation of the TPQGel prepolymer mixture: GelMA (10% w/v), TPQ nanoparticles (5% w/v), and photoinitiator (0.5% LAP) were mixed in proportion. The mixture was gently vortexed to ensure homogeneity and then stored in the dark for later use.

(2) Hydrogel construction in the upper chamber of the Transwell system: Prepolymer mixture was added to the upper chamber of the Transwell system (pore size, 8 μm; diameter, 6.5 mm), with 50 μL per well used to cover the porous membrane surface. The solution was then crosslinked by exposure to 405 nm ultraviolet light (intensity 10 mW/cm²) for 30 s to form the hydroge.

(3) Posttreatment of the hydrogel: The hydrogel was washed three times with sterile PBS to remove unccrosslinked components. The mixture was then equilibrated with complete medium (e.g., α-MEM + 10% FBS) for 2 h.

(4) Cell seeding in the lower chamber: The lower chamber was filled with 550 μL of cell-containing medium (e.g., HUVECs or MC-3T3-E1 cells at a density of 5×10^4 cells per well). The upper chamber was filled with 200 μL of cell-free medium to create a liquid level difference that drives molecular diffusion.

(5) Coculture and detection: The setup was cultured at 37 °C with 5% CO_2. The medium was changed every 24 h. Cells were collected at the designated time points (e.g., 24 h, 48 h, 72 h) for analysis of migration, proliferation (CCK-8), or differentiation (qPCR/WB) as per the experimental design.

Evaluation of in vitro cytocompatibility

(1) Cell Viability Quantification: A Transwell co-culture model (polycarbonate membrane, 0.4 μm pore) was established to evaluate hydrogel cytocompatibility. MC-3T3-E1 preosteoblasts and HUVECs (5 × 10^4 cells/well) were cultured in the lower chamber, while experimental hydrogels (Φ6 × 2 mm) occupied the upper compartment. At designated intervals (24, 72, 120 h), cellular metabolic activity was determined using CCK-8 assay: 10% (v/v) reagent (Dojindo Laboratories) was administered to each well, followed by 1 h incubation (37 °C, 5% CO_2). Absorbance at 450 nm was quantified using a multimode microplate reader (SpectraMax iD5, Molecular Devices).

(2) Morphological Characterization: Post 72 h incubation, viability was verified through dual fluorescence staining (Calcein-AM/PI, Thermo Fisher) with 15 min

exposure. Live/dead cell distributions were imaged under laser scanning confocal microscopy (LSM 880, Zeiss). For cytoskeletal architecture analysis, fixed cells were permeabilized (0.1% Triton X-100, 5 min), stained with Alexa Fluor 488-phalloidin (1:200, Invitrogen) and DAPI (5 μg/mL). Cellular spreading parameters (projected area, circularity) were quantified using ImageJ v1.53t with built-in particle analysis algorithms.

In vitro Immunomodulatory evaluation

(1) Macrophage stimulation and coculture with hydrogels: RAW264.7 macrophages preconditioned with lipopolysaccharide (LPS, 10 ng/mL, 24 h) were plated in the lower chamber of Transwell® systems (Corning, 3.0 μm pore). Test hydrogels (Φ6 × 2 mm) were positioned in the upper inserts, establishing indirect contact co-culture for 72 h (37 °C, 5% CO_2). Morphodynamic alterations were captured through z-axis reconstructed confocal imaging (LSM 900, Zeiss; 40× oil objective).

(2) Detached cells underwent Fc receptor blocking (TrueStain FcX, BioLegend) prior to 30-min incubation with fluorochrome-conjugated antibodies: anti-CD86-APC (Clone GL-1, 1:100, E-AB-F0994E) and anti-CD206-PE (Clone MR6F3, 1:50, F-AB-F1135C). Flow cytometric acquisition (CytoFLEX LX, Beckman Coulter) employed standardized voltage settings with compensation controls. Data analysis via FlowJo v10.8.1 (BD Biosciences).

(3) Fixed macrophages (4% PFA, 15 min) were permeabilized (0.3% Triton X-100) and blocked with 5% BSA. Primary antibodies (CD86/CD206, 1:200) were applied overnight (4 °C), followed by Alexa Fluor-conjugated secondary antibodies (1:500, 2 h). Nuclei were counterstained with DAPI (Thermo Fisher). Fluorescence intensity quantification utilized ImageJ's integrated density measurement with background subtraction (ROI = 50 × 50 μm^2).

In vitro evaluation of angiogenic activity

(1) Wound Healing Assay: HUVECs (2 × 10^5 cells/well) were cultured in 6-well plates to form confluent monolayers. Mechanical wounding was performed using sterile 200 μL pipette tips, generating standardized scratches (width = 800 ± 50 μm). After PBS washing to remove debris, wound closure dynamics were monitored through time-lapse phase-contrast microscopy (Nikon Eclipse Ti2, 10× objective) over 24 h. Migration rates were calculated using ImageJ's MRI Wound Healing Tool plugin, expressed as percentage closure relative to initial wound area.

(2) Transwell Migration Assay: Transwell® chambers (8 μm pore, Corning) were employed with serum-free endothelial basal medium in lower compartments. HUVEC suspensions (5 × 10^4 cells/200 μL) were loaded into upper chambers. Following 24 h chemoattraction, transmigrated cells underwent methanol fixation and 0.1% crystal violet staining (Sigma-Aldrich). 3 random fields per membrane were imaged (Olympus IX83, 20×), with cell counts normalized to control groups.

(3) In vitro angiogenesis assay: Growth factor-reduced Matrigel (Corning, 150 μL/well) was polymerized (37 °C, 30 min) in μ-Slide Angiogenesis plates (Ibidi). HUVECs (1 × 10^4 cells/well) were seeded and tube formation recorded hourly for 7 h using automated live-cell imaging (Incucyte S3). Network parameters (total tube length, branch points) were quantified via AngioTool v2.0 (NCI).

(4) Immunofluorescence Staining: Immunofluorescent detection of CD31/VEGF employed Alexa Fluor 647-conjugated antibodies (1:200, Abcam), with z-stack confocal images (20 μm depth) analyzed for fluorescence colocalization (Pearson's coefficient) using Imaris 9.9.

In vitro evaluation of osteogenic differentiation

(1) Wound Healing Assay: MC-3T3-E1 preosteoblasts (2 × 10^5 cells/well) were cultured in 6-well Transwell® plates (Corning, 3.0 μm pore) to form confluent monolayers. Standardized scratch wounds (width = 1000 ± 50 μm) were created using silicon-tipped scratchers (Culture-Insert 2 Well, Ibidi). Experimental hydrogels were positioned in upper chambers with serum-free α-MEM in lower compartments. Migration rates were calculated using ImageJ's MRI Wound Healing Tool plugin, expressed as percentage closure relative to initial wound area.

(2) Cell suspensions (5 × 10^4 cells/200 μL serum-free medium) were loaded into 24-well Transwell® inserts (8 μm pore). After 24 h chemoattraction, migrated cells underwent methanol fixation and 0.1% crystal violet staining. 3 non-overlapping fields per membrane were imaged (20×, Nikon Eclipse Ts2), with automated cell counting via ImageJ's Analyze Particles function (size threshold = 50–500 μm^2).

(3) Osteogenic Differentiation Assay: Cells were maintained in osteogenic induction medium (10% FBS, 0.1 μM dexamethasone, 10 mM β-glycerophosphate, 50 μg/mL L-ascorbic acid) with triweekly medium renewal. At day 7, ALP activity was determined through: (1) BCIP/NBT chromogenic staining (Beyotime C3206) imaged with phase-contrast microscopy (Leica DMi8). (2) Quantitative measurement via p-nitrophenyl phosphate hydrolysis (405 nm) normalized to total protein (BCA assay, Pierce™). Matrix mineralization at day 14 was assessed by: (1) 2% Alizarin Red S (pH 4.2) staining (Sigma-Aldrich). (2) Quantitative dissolution in 10% CPC (OD562 nm) with hydroxyapatite standard curve.

(4) Molecular Signature Characterization: Post 7-day culture, total protein was extracted using RIPA buffer (25 mM Tris-HCl, 150 mM NaCl, 1% NP-40) supplemented with protease/phosphatase inhibitors (Roche). Western

blotting employed 12% SDS-PAGE with anti-RUNX2 (1:1000, Abcam ab236639) and anti-OPN (1:500, Santa Cruz sc-73631) antibodies.

Establishment and treatment of the femoral defect model in rats

(1) Animal Model and Grouping: Male Sprague-Dawley rats (8 weeks, 250 ± 15 g) were acclimatized for 7 days under standard conditions (22 ± 1 °C, 12/12 light cycle). Subjects were stratified into three cohorts ($n = 6$/group) using block randomization: (1) Sham Control: Defect creation without implantation. (2) TPGel: Tricalcium phosphate-polydopamine hydrogel implantation. (3) TPQGel: QK peptide-functionalized TPGel implantation.

(2) Surgical Procedure: General anesthesia was induced via intraperitoneal sodium pentobarbital (35 mg/kg) with perioperative analgesia (buprenorphine SR, 1 mg/kg SC). Following aseptic preparation (chlorhexidine scrub, iodophor drape), a lateral para-patellar approach exposed the left femoral metaphysis. A critical-size defect ($5 \times 5 \times 3$ mm^3) was created using trephine burs (2.3 mm diameter, 30,000 rpm) under saline irrigation. Hydrogel scaffolds (γ-irradiated sterilization) were precisely fitted into defects using custom 3D-printed guides. Wound closure employed layered suturing (4 – 0 Vicryl® for muscle, 5 – 0 Prolene® for skin). Postoperative monitoring included daily weight tracking and thermal support until ambulation recovery. The experimental protocol was reviewed and approved by the Animal Ethics Committee of Shanghai Public Health Clinical Center (approval number 2023-A032-01).

Gross observation and radiological evaluation

(1) Euthanasia and Sample Collection: Terminal anesthesia was induced via pentobarbital overdose (100 mg/kg IP), followed by transcardial perfusion with heparinized saline. Bilateral femora were dissected through anatomical layer separation, preserving periosteal integrity. Specimens underwent sequential processing: (1) Primary fixation: 48 h immersion in 4% PFA (0.1 M PBS, pH 7.4). (2) Decalcification: 14-day EDTA treatment (10% w/v, 4 °C) with weekly solution renewal. (3) Stabilization: Cryopreservation in 30% sucrose/PBS (72 h).

(2) Quantitative Bone Analysis: Following the imaging procedures, the BV/TV and Tb.Th were determined via specialized software for quantitative comparison. These parameters provide insights into the structural integrity of bone and the efficacy of the treatments administered.

Histological examination

(1) Tissue Harvesting and Processing: At 3-week endpoint, transcardially perfused femurs were dissected and immersion-fixed in neutral buffered 4% paraformaldehyde (72 h, 4 °C). Decalcification proceeded in 10% EDTA (pH 7.4, 4 °C) with solution renewal every 72 h until radiographic confirmation (Faxitron MX-20). Dehydrated specimens (ethanol-xylene series) were paraffin-embedded (Leica EG1160) and sectioned coronally at 5 μm thickness (RM2255 microtome). Sections underwent modified Masson staining and anti-OPN immunohistochemistryn using automated platforms (BenchMark ULTRA, Ventana).

(2) Organ Biocompatibility Assessment: Major organs (heart, liver, spleen, lungs, kidneys) were harvested at 12-week post-implantation. Tissues underwent: (1) Gross pathology scoring (0–4 scale: congestion/necrosis). (2) Histopathological processing: 4 μm sections stained with H&E.

(3) Subcutaneous Vascularization Study: To investigate the subcutaneous vascularization effects of the TPQGel, 12 SD rats were randomly selected and equally divided into two groups. One group received subcutaneous implantation of the TPQGel hydrogel, while the other served as a Control. Vascularization at the implantation sites was evaluated at 5 and 10 days postimplantation.

Bulk RNA sequencing analysis of transcriptional differences in Raw 264.7 cell from male and female mice

Total RNA was isolated from mouse Raw 264.7 cell and enriched for mRNA using Oligo(dT) magnetic beads. Following RNA fragmentation, first-strand cDNA synthesis was performed using random hexamer primers and reverse transcriptase with RNA as the template. The second-strand cDNA was subsequently synthesized using the first-strand cDNA as a template. Libraries were prepared and subjected to paired-end sequencing on an Illumina next-generation sequencing (NGS) platform. Raw sequencing reads were rigorously filtered to retain high-quality clean data for downstream analyses. Differentially expressed genes (DEGs) between sexes were identified using the DESeq2 algorithm, and pathway enrichment analysis was conducted via the Metascape web-based platform.

Statistical analysis

All the experiments were performed with three or more replications. The results are expressed as the means ± SDs. Statistical analysis was performed via SPSS software (version 21, USA). For comparisons between groups, repeated data were examined via ANOVA. Statistical significance was determined according to the following p values: $^{*}P < 0.05$, $^{**}P < 0.01$; $^{\#}P < 0.05$, $^{\#\#}P < 0.01$. All the graphs were prepared via GraphPad Prism (version 9.4.1, USA).

Supplementary Information

The online version contains supplementary material available at https://doi.org/10.1186/s12951-025-03358-2.

Supplementary Material 1

Acknowledgements
We are grateful to Shanghai Bioprofile Technology Company Ltd.

Author contributions
H.Z.,Y.W., W.Q., and X.H. designed the content and wrote the first draft; H.Q.,K.X, prepared Fig. 1 and 2, 3 L.D.,L.Y.,prepared Fig. 4, 5 and 6 B.Y. prepared Fig. 7, 8 J.G.,T.Z.,Z.Y. were responsible for supervision of the entireproject as the corresponding author.(Z.Y.as the primary corresponding author).

Funding
This work was supported by the National Natural Science Foundation of China (Award Numbers 8247326 and 82072051) and the National Key Laboratory 2024 Basic Medicine Innovation Open project (Award Number JCKFKT-MS-006).

Data availability
No datasets were generated or analysed during the current study.

Declarations

Ethical approval
The experimental protocol was reviewed and approved by the Animal Ethics Committee of Shanghai Public Health Clinical Center (approval number 2023-A032-01).

Competing interests
The authors declare no competing interests.

Author details
[1]Department of Orthopedics, Jinshan Hospital, Fudan University, Shanghai 201508, China
[2]Department of General Surgery, Jinshan Hospital, Fudan University, Shanghai 201508, China
[3]Changhai Clinical Research Unit, Shanghai Changhai Hospital, Naval Medical University, Shanghai 200433, China
[4]Digestive Endoscopy Center, School of Medicine, Shanghai Tongren Hospital, Shanghai Jiao Tong University, Shanghai 200336, China
[5]Biological Safety Protection 3-Level Laboratory, Guangxi Medical University, Nanning, Guangxi Zhuang 530021, China
[6]Shanghai Key Laboratory of Nautical Medicine and Translation of Drugs and Medical Devices, Shanghai 200433, China

Received: 4 February 2025 / Accepted: 26 March 2025
Published online: 07 April 2025

References

1. Sun L, Niu H, Wu Y, Dong S, Li X, Kim BYS, Liu C, Ma Y, Jiang W, Yuan Y. Bio-integrated scaffold facilitates large bone regeneration dominated by endochondral ossification. Bioactive Mater. 2024;35:208–27. https://doi.org/10.1016/j.bioactmat.2024.01.019.
2. Wu M, Liu H, Zhu Y, Chen F, Chen Z, Guo L, Wu P, Li G, Zhang C, Wei R, et al. Mild Photothermal-Stimulation based on injectable and photocurable hydrogels orchestrates Immunomodulation and osteogenesis for High-Performance bone regeneration. Small. 2023;19. https://doi.org/10.1002/smll.202300111.
3. Liu Q, Zhang S, Shi L, Shi J, Sun C, Wang J, Zhou W, Zhou H, Shan F, Wang H, et al. Osteogenic induction and Anti-Inflammatory effects of Calcium-Chlorogenic acid nanoparticles remodel the osteoimmunology microenvironment for accelerating bone repair. Adv Healthc Mater. 2024;13. https://doi.org/10.1002/adhm.202401114.
4. Han S, Yang H, Ni X, Deng Y, Li Z, Xing X, Du M. Programmed release of vascular endothelial growth factor and exosome from injectable Chitosan nanofibrous microsphere-based PLGA-PEG-PLGA hydrogel for enhanced bone regeneration. Int J Biol Macromol. 2023;253. https://doi.org/10.1016/j.ijbiomac.2023.126721.
5. van der Heide D, Cidonio G, Stoddart MJ, D'Este M. 3D printing of inorganic-biopolymer composites for bone regeneration. Biofabrication. 2022;14. https://doi.org/10.1088/1758-5090/ac8cb2.
6. Du H, Li B, Yu R, Lu X, Li C, Zhang H, Yang F, Zhao R, Bao W, Yin X, et al. ETV2 regulating PHD2-HIF-1α axis controls metabolism reprogramming promotes vascularized bone regeneration. Bioactive Mater. 2024;37:222–38. https://doi.org/10.1016/j.bioactmat.2024.02.014.
7. Li R, Zhou C, Chen J, Luo H, Li R, Chen D, Zou X, Wang W. Synergistic osteogenic and angiogenic effects of KP and QK peptides incorporated with an injectable and self-healing hydrogel for efficient bone regeneration. Bioactive Mater. 2022;18:267–83. https://doi.org/10.1016/j.bioactmat.2022.02.011.
8. Li J, Ma J, Feng Q, Xie E, Meng Q, Shu W, Wu J, Bian L, Han F, Li B. Building osteogenic microenvironments with a Double-Network composite hydrogel for bone repair. Research. 2023;6. https://doi.org/10.34133/research.0021.
9. Chen Z, Wang L, Guo C, Qiu M, Cheng L, Chen K, Qi J, Deng L, He C, Li X, et al. Vascularized polypeptide hydrogel modulates macrophage polarization for wound healing. Acta Biomater. 2023;155:218–34. https://doi.org/10.1016/j.actbio.2022.11.002.
10. Lai Y, Zhang T, Yin X, Zhu C, Du Y, Li Z, Gao J. An antibiotic-free platform for eliminating persistent Helicobacter pylori infection without disrupting gut microbiota. Acta Pharm Sin B. 2024;14:3184–204. https://doi.org/10.1016/j.apsb.2024.03.014.
11. Zhang H, Wang Y, Qiang H, Leng D, Yang L, Hu X, Chen F, Zhang T, Gao J, Yu Z. Exploring the frontiers: the potential and challenges of bioactive scaffolds in osteosarcoma treatment and bone regeneration. Mater Today Bio. 2024;29. https://doi.org/10.1016/j.mtbio.2024.101276.
12. Trompet D, Melis S, Chagin AS, Maes C. Skeletal stem and progenitor cells in bone development and repair. J Bone Miner Res. 2024;39:633–54. https://doi.org/10.1093/jbmr/zjae069.
13. Zeng J, Sun P, Zhao Y, Fang X, Wu Z, Qi X. Bone mesenchymal stem cell-derived exosomes involved co-delivery and synergism effect with Icariin via mussel-inspired multifunctional hydrogel for cartilage protection. Asian J Pharm Sci. 2023;18. https://doi.org/10.1016/j.ajps.2023.100799.
14. Han Y, Dal-Fabbro R, Mahmoud AH, Rahimnejad M, Xu J, Castilho M, Dissanayaka WL, Bottino MC. GelMA/TCP nanocomposite scaffold for vital pulp therapy. Acta Biomater. 2024;173:495–508. https://doi.org/10.1016/j.actbio.2023.11.005.
15. Lu T, Li G, Zhang L, Yuan X, Wu T, Ye J. Optimizing silicon doping levels for enhanced osteogenic and angiogenic properties of 3D-printed biphasic calcium phosphate scaffolds: an in vitro screening and in vivo validation study. Mater Today Bio. 2024;28. https://doi.org/10.1016/j.mtbio.2024.101203.
16. Yin X, Lai Y, Zhang X, Zhang T, Tian J, Du Y, Li Z, Gao J. Targeted sonodynamic therapy platform for holistic integrative Helicobacter pylori therapy. Adv Sci (Weinh). 2024;e2408583. https://doi.org/10.1002/advs.202408583.
17. Lyu B, Zhang Y, Ren J, Gao D, Zhou Y, Wang Y, Ma J. High mechanical properties nanocomposite hydrogel achieved based on montmorillonite and tailored microgel suspensions reinforcing Polyacryamide networks. Colloids Surf A. 2024;687. https://doi.org/10.1016/j.colsurfa.2024.133566.
18. Du H, Li W, Li X, Qiu Z, Ding J, Zhang Y. Optimizing the biocompatibility of PLLA stent materials: strategy with biomimetic coating. Int J Nanomed. 2024;19:5157–72. https://doi.org/10.2147/ijn.S462691.
19. Fan L, Ma X, Liu B, Yang Y, Yang Y, Ren T, Li Y. Antioxidant-Engineered Milk-Derived extracellular vesicles for accelerating wound healing via regulation of the PI3K-AKT signaling pathway. Adv Healthc Mater. 2023;12. https://doi.org/10.1002/adhm.202301865.
20. Wu M, Chen F, Wu P, Yang Z, Zhang S, Xiao L, Deng Z, Zhang C, Chen Y, Cai L. Bioinspired Redwood-Like scaffolds coordinated by in Situ-Generated Silica-Containing hybrid nanocoatings promote angiogenesis and osteogenesis both in vitro and in vivo. Adv Healthc Mater. 2021;10. https://doi.org/10.1002/adhm.202101591.
21. Shapouri-Moghaddam A, Mohammadian S, Vazini H, Taghadosi M, Esmaeili SA, Mardani F, Seifi B, Mohammadi A, Afshari JT, Sahebkar A. Macrophage plasticity, polarization, and function in health and disease. J Cell Physiol. 2018;233:6425–40. https://doi.org/10.1002/jcp.26429.
22. Chen S, Lu K, Hou Y, You Z, Shu C, Wei X, Wu T, Shi N, Zhang G, Wu J, et al. YY1 complex in M2 macrophage promotes prostate cancer progression by upregulating IL-6. J Immunother Cancer. 2023;11. https://doi.org/10.1136/jitc-2022-006020.
23. Ma Y, Sun L, Zhang J, Chiang CI, Pan J, Wang X, Kwak KJ, Li H, Zhao R, Rima XY, et al. Exosomal mRNAs for Angiogenic–Osteogenic coupled bone repair. Adv Sci. 2023;10. https://doi.org/10.1002/advs.202302622.

24. Zhao Y, Xie L. Unique bone marrow blood vessels couple angiogenesis and osteogenesis in bone homeostasis and diseases. Ann N Y Acad Sci. 2020;1474:5–14. https://doi.org/10.1111/nyas.14348.
25. Zhang X, Zhang M, Cui H, Zhang T, Zhang Z, Li J, Zhou J, Jiang X, Liu C, Gao J. Integrated copper Nanomaterials-Decorated microsphere photothermal platform for comprehensive melanoma treatment. Small Struct. 2024;5. https://doi.org/10.1002/sstr.202400028.
26. Xu W, Wu Y, Lu H, Zhang X, Zhu Y, Liu S, Zhang Z, Ye J, Yang W. Injectable hydrogel encapsulated with VEGF-mimetic peptide-loaded nanoliposomes promotes peripheral nerve repair in vivo. Acta Biomater. 2023;160:225–38. https://doi.org/10.1016/j.actbio.2023.02.004.
27. Xia B, Deng Y, Lv Y, Chen G. Stem cell recruitment based on scaffold features for bone tissue engineering. Biomaterials Sci. 2021;9:1189–203. https://doi.org/10.1039/d0bm01591a.
28. Chen Z, Lv Z, Zhuang Y, Saiding Q, Yang W, Xiong W, Zhang Z, Chen H, Cui W, Zhang Y. Mechanical Signal-Tailored hydrogel microspheres recruit and train stem cells for precise differentiation. Adv Mater. 2023;35. https://doi.org/10.1002/adma.202300180.
29. Ding T, Kang W, Li J, Yu L, Ge S. An in situ tissue engineering scaffold with growth factors combining angiogenesis and osteoimmunomodulatory functions for advanced periodontal bone regeneration. J Nanobiotechnol. 2021;19. https://doi.org/10.1186/s12951-021-00992-4.
30. Mao M, Zhu S, Zhang L, Liu F, Kong L, Xue Y, Rotello VM, Han Y. An extracellular Matrix-like surface for Zn alloy to enhance bone regeneration. ACS Appl Mater Interfaces. 2022;14:43955–64. https://doi.org/10.1021/acsami.2c12513.
31. Wu Z, Bai J, Ge G, Wang T, Feng S, Ma Q, Liang X, Li W, Zhang W, Xu Y, et al. Regulating macrophage polarization in high glucose microenvironment using Lithium-Modified Bioglass-Hydrogel for diabetic bone regeneration. Adv Healthc Mater. 2022;11. https://doi.org/10.1002/adhm.202200298.
32. Wang Y, Lin Q, Zhang H, Wang S, Cui J, Hu Y, Liu J, Li M, Zhang K, Zhou F, et al. M2 macrophage-derived exosomes promote diabetic fracture healing by acting as an Immunomodulator. Bioactive Mater. 2023;28:273–83. https://doi.org/10.1016/j.bioactmat.2023.05.018.
33. Wu Y, Li M, He R, Xiao L, Liu S, Chen K, Qiang H, Ji K, Li L, Yin Y, et al. Photosynthetic live microorganism-incorporated hydrogels promote diabetic wound healing via self-powering and oxygen production. Chem Eng J. 2024. https://doi.org/10.1016/j.cej.2024.149545.
34. Lin Z, Chen Z, Chen Y, Yang N, Shi J, Tang Z, Zhang C, Lin H, Yin J. Hydrogenated silicene nanosheet functionalized scaffold enables immuno-bone remodeling. Explor (Beijing). 2023;3. https://doi.org/10.1002/EXP.20220149.
35. Han N, Liu Y, Du J, Xu J, Guo L, Liu Y. Regulation of the host immune microenvironment in periodontitis and periodontal bone remodeling. Int J Mol Sci. 2023;24. https://doi.org/10.3390/ijms24043158.
36. Gao J, Zhai Y, Lu W, Jiang X, Zhou J, Wu L, Du L, Ou C, Zhang X, He H, et al. ROS-sensitive PD-L1 SiRNA cationic Selenide nanogels for self-inhibition of autophagy and prevention of immune escape. Bioact Mater. 2024;41:597–610. https://doi.org/10.1016/j.bioactmat.2024.08.013.
37. Lu J, Gao X, Wang S, He Y, Ma X, Zhang T, Liu X. Advanced strategies to evade the mononuclear phagocyte system clearance of nanomaterials. Explor (Beijing). 2023;3. https://doi.org/10.1002/EXP.20220045.
38. Wang Y, Zhan J, Huang J, Wang X, Chen Z, Yang Z, Li J. Dynamic responsiveness of self-assembling peptide-based nano-drug systems. Interdisciplinary Med. 2023;1. https://doi.org/10.1002/inmd.20220005.
39. Zheng L, Interdisciplinary M. Bridge the gaps in medical interdisciplinary research. Interdisciplinary Med. 2023;1. https://doi.org/10.1002/inmd.20230001.
40. Arif ZU, Khalid MY, Noroozi R, Hossain M, Shi HH, Tariq A, Ramakrishna S, Umer R. Additive manufacturing of sustainable biomaterials for biomedical applications. Asian J Pharm Sci. 2023;18. https://doi.org/10.1016/j.ajps.2023.100812.

Publisher's note